Zhao et al. *Zool. Res.* 2026, 47(4): 1106−1123
https://doi.org/10.24272/j.issn.2095-8137.2025.573
https://cstr.cn/32248.14.zr.2025.573

ZR | Zoological Research

Article Open Access

zDHHC20b-mediated TRIF palmitoylation drives infection-induced necroptosis through the TRIF-RIPK3 axis in teleost monocytes/macrophages

Zi-Yue Zhao[1,2,3,#], Chen-Jie Fei[1,2,3,#], Ting-Fang Zhu[1,2,3], Xi-Zhi Shi[1,2,3], Jian-Zhong Shao[4], Li Nie[1,2,3,*], Jiong Chen[1,2,3,*]

[1] *State Key Laboratory for Quality and Safety of Agro-Products*, *Ningbo University*, *Ningbo*, *Zhejiang* 315211, *China*

[2] *Laboratory of Biochemistry and Molecular Biology*, *School of Marine Sciences*, *Ningbo University*, *Ningbo*, *Zhejiang* 315211, *China*

[3] *Key Laboratory of Aquaculture Biotechnology of Ministry of Education*, *Ningbo University*, *Ningbo*, *Zhejiang* 315211, *China*

[4] *College of Life Sciences*, *Key Laboratory for Cell and Gene Engineering of Zhejiang Province*, *Zhejiang University*, *Hangzhou*, *Zhejiang* 310058, *China*

ABSTRACT

Palmitoylation is a reversible post-translational modification that regulates protein trafficking, stability, and function, yet its contribution to immune cell death in teleosts remains largely unknown. Using large yellow croaker (*Larimichthys crocea*) as a teleost model, this study identified the palmitoyltransferase zDHHC20b (*Lcz*DHHC20b) as the infection-responsive zDHHC20 paralog that promoted necroptosis in monocytes/macrophages (MO/MΦ) during *Pseudomonas plecoglossicida* infection. *Lcz*DHHC20b knockdown disrupted inflammatory cytokine regulation and markedly reduced necroptotic cell death. Acyl-biotin exchange assays combined with liquid chromatography-tandem mass spectrometry identified TIR-domain-containing adapter-inducing interferon-β (TRIF), a central adaptor in innate immune signaling, as a cell death-related palmitoylation substrate of *Lcz*DHHC20b. Infection progressively increased TRIF palmitoylation at Cys92 and Cys142, which enhanced recruitment of receptor-interacting serine/threonine kinase 3 (RIPK3), promoted phosphorylation of RIPK3 and mixed lineage kinase domain-like protein (MLKL), and activated necroptosis. *Lcz*DHHC20b knockdown or pharmacological inhibition of palmitoylation with 2-bromopalmitate (2-BP) impaired TRIF-RIPK3 complex assembly and suppressed downstream necroptotic signaling. Palmitoylation-deficient TRIF also exhibited reduced localization to endoplasmic reticulum- and trans-Golgi network-associated compartments, suggesting that palmitoylation contributes to the spatial organization of TRIF-dependent signaling. These findings provide the first evidence of TRIF palmitoylation and establish this modification as a previously unrecognized post-translational mechanism regulating TRIF-mediated immune cell death. The identified *Lcz*DHHC20b-TRIF-RIPK3 axis further defines a lipid-dependent pathway that controls necroptosis in teleost macrophages and shapes host-pathogen interactions during bacterial infection.

Keywords: Palmitoylation; TRIF; zDHHC20b; RIPK3; Necroptosis; Monocytes/macrophages

INTRODUCTION

Necroptosis is a regulated lytic form of programmed cell death that contributes to host defense against microbial infection and to tissue damage under sterile inflammatory conditions. Unlike apoptosis, necroptosis disrupts plasma membrane integrity and releases intracellular danger-associated molecular patterns (DAMPs), thereby amplifying immune responses and inflammatory signaling (Dhuriya & Sharma, 2018). Necroptosis can be triggered by multiple innate immune pathways, including those mediated by retinoic acid-inducible gene I-like receptors, Toll-like receptors (TLRs), and death receptors (Newton & Manning, 2016). Despite distinct upstream recognition and signaling mechanisms, these pathways ultimately activate receptor-interacting serine/threonine kinase 3 (RIPK3), with receptor-interacting serine/threonine kinase 1 (RIPK1) often mediating this activation downstream of death receptor stimulation (Newton, 2015). Activated RIPK3 phosphorylates mixed lineage kinase domain-like protein (MLKL), promoting its oligomerization and translocation to the plasma membrane, and the resulting membrane permeabilization leads to cell swelling, membrane rupture, and lytic death (Khan et al., 2014).

However, RIPK1 is not an obligatory activator of

Received: 28 April 2026; Accepted: 14 May 2026; Online: 15 May 2026

Foundation items: This work was supported by the National Natural Science Foundation of China (U25A20726) and Natural Science Foundation of Zhejiang Province (LZYQ25C190001)

[#]Authors contributed equally to this work

*Corresponding authors, E-mail: nieli@nbu.edu.cn; chenjiong@nbu.edu.cn

necroptosis. Other proteins containing a RIP homotypic interaction motif (RHIM), including TIR-domain-containing adapter-inducing interferon-β (TRIF) and DNA-dependent activator of interferon regulatory factors (DAI, also known as ZBP1), can directly recruit RIPK3 through RHIM-mediated interactions and initiate MLKL-dependent necroptosis (Lu et al., 2024). Among these pathways, TLR-mediated necroptosis represents a prominent RIPK1-independent pathway. TLR3 detects double-stranded RNA (dsRNA) within endosomal compartments, whereas TLR4 recognizes bacterial lipopolysaccharide (LPS) and engages TRIF to recruit and activate RIPK3 via RHIM domain interactions. This molecular engagement activates the RIPK3-MLKL cascade and drives necroptotic cell death.

Palmitoylation is a prevalent and reversible post-translational lipid modification estimated to affect 30%–40% of the human proteome (Chamberlain & Shipston, 2015; Mesquita et al., 2024; Zaballa and van der Goot, 2018). The reaction involves covalent attachment of a 16-carbon saturated fatty acyl chain, usually referred to as a palmitoyl group, to selected cysteine residues via a thioester linkage (Fang et al., 2006; Greaves et al., 2011). This reversible modification regulates a wide range of cellular processes, including signal transduction, membrane trafficking, cell migration, and protein complex assembly (Chen et al., 2018; Shang et al., 2022). Palmitoylation is catalyzed through a two-step mechanism by zinc-finger DHHC motif-containing palmitoyltransferases (zDHHCs). A zDHHC enzyme first binds fatty acyl-coenzyme A (acyl-CoA) and undergoes autoacylation at the catalytic cysteine within the DHHC motif, releasing free CoA. The acyl group is then transferred from the enzyme to a cysteine residue in the protein substrate (Gottlieb & Linder, 2017; Jiang et al., 2018; Khoury et al., 2011). The mammalian zDHHC family comprises 23 members in humans and 24 in mice, all of which contain a conserved cysteine-rich DHHC domain exposed to the cytoplasm and at least four transmembrane segments (Fukata et al., 2004; Politis et al., 2005; Rana et al., 2018; Stix et al., 2020).

Recent studies have uncovered critical roles for palmitoylation as a regulator of necroptosis in mammals. Notably, zDHHC5-driven palmitoylation of RIPK1 has been shown to promote oligomerization of the kinase domain, thereby enhancing RIPK1 kinase activity and facilitating necroptotic cell death (Zhang et al., 2024b). In addition, zDHHC21-mediated palmitoylation of MLKL similarly supports retention of MLKL at the plasma membrane, thereby promoting membrane permeabilization during the terminal phase of necroptosis (Pradhan et al., 2024). Despite these advances, whether palmitoylation also regulates other central components of the necroptotic pathway, including TRIF and ZBP1, has yet to be resolved. Moreover, evidence for this regulatory mechanism has come almost exclusively from mammalian systems, whereas its evolutionary conservation and immunological significance in nonmammalian vertebrates remain unclear, despite the presence of conserved necroptotic machinery and frequent pathogenic challenge in teleost fish (Ding et al., 2021; Hao et al., 2024; Qi et al., 2021).

The zDHHC palmitoyltransferase repertoire in teleosts remains poorly characterized. In zebrafish, five zDHHC isoforms have been reported to regulate biological processes ranging from embryogenesis to neuronal differentiation (Chen et al., 2014; Shi et al., 2015, 2016; Wang et al., 2015). However, investigations into the immunological functions of teleost zDHHC enzymes are limited. zDHHC1 is currently the only family member linked to antiviral defense in fish, with evidence from both grass carp and sea bass models (Xu et al., 2017). Our previous work in large yellow croaker (*Larimichthys crocea*, *Lc*), an economically important marine species, identified 22 zDHHC family members denoted as *Lc*zDHHC1–24, excluding isoforms 10 and 19 (Dai et al., 2024). Transcriptional screening further revealed marked induction of *Lc*zDHHC20b in monocytes/macrophages (MO/MΦ) following *Pseudomonas plecoglossicida* infection (Dai et al., 2024). However, the precise function of *Lc*zDHHC20b in antibacterial host defense and immune cell fate has not yet been elucidated.

In this study, *Lc*zDHHC20b was identified as the infection-responsive zDHHC20 paralog in large yellow croaker and was shown to regulate necroptosis in MO/MΦ cells during *P. plecoglossicida* infection. *Lc*zDHHC20b, but not its paralog *Lc*zDHHC20a, promoted TRIF palmitoylation, enhanced assembly of the TRIF-RIPK3 complex, and activated downstream RIPK3-MLKL necroptotic signaling. Cys92 and Cys142 were identified as major residues required for *Lc*TRIF palmitoylation, and disruption of this modification altered intracellular TRIF localization, indicating that palmitoylation contributes to the spatial organization of TRIF-dependent signaling. To the best of our knowledge, these findings provide the first evidence in any species that TRIF undergoes palmitoylation and reveal a previously unknown post-translational mechanism regulating TRIF-dependent necroptosis. The identified *Lc*zDHHC20b-TRIF-RIPK3 axis defines a lipid-dependent regulatory pathway in teleost innate immunity and provides mechanistic insight into how palmitoylation shapes host-pathogen interactions during bacterial infection.

MATERIALS AND METHODS

Cell lines and culture conditions

HEK293T and HeLa cells were maintained in Dulbecco's Modified Eagle Medium (DMEM, #11966025, Gibco, Thermo Fisher Scientific, USA) supplemented with 10% fetal bovine serum (FBS, #26140079, Thermo Fisher Scientific, USA) and 1% penicillin-streptomycin (#15140148, Thermo Fisher Scientific, USA). Cells were cultured in a humidified incubator at 37°C in 5% CO_2.

*Lc*zDHHC20 gene cloning and bioinformatics analysis

*Lc*zDHHC20a and *Lc*zDHHC20b were amplified by reverse transcription polymerase chain reaction (RT-PCR) using PrimeSTAR GXL DNA polymerase (#R051A, TaKaRa, Japan), with primers designed according to sequences retrieved from the National Center for Biotechnology Information (NCBI) database (Supplementary Table S1). Multiple sequence alignment was performed using Clustal Omega in MEGA v.12 (Kumar et al., 2024). Phylogenetic relationships were inferred from amino acid sequences. The optimal amino acid substitution model was selected using the "Find Best Protein Model (ML)" function in MEGA v.12 according to the lowest Bayesian Information Criterion (BIC) value. A maximum-likelihood phylogenetic tree was reconstructed using the selected model, with 1 000 bootstrap replicates and the SPR heuristic search method (Keklik, 2023). Functional motifs were predicted using Pfam v.31.0 (Punta et al., 2012) and the NCBI Conserved Domain Database. Tertiary structures were generated using AlphaFold 3 (Abramson et al., 2024) and visualized in PyMOL v.3.1

(Osipovitch et al., 2015). All sequences are listed in Supplementary Tables S2, S3.

Experimental infection and tissue sampling

Healthy large yellow croakers (10–12 months old, 100–120 g, *n*=120) were obtained from Xiangshan Harbor Aquatic Seed (Ningbo, China) and acclimated for 2 weeks in a recirculating seawater system at 18–20°C. Fish were then intraperitoneally challenged with logarithmic-phase *P. plecoglossicida* strain NZBD9 (Hu et al., 2014) at 5×10^4 CFU/100 g fish, whereas control fish received phosphate-buffered saline (PBS). Tissue samples were collected at 0, 6, 12, 24, 48, and 72 h post-infection (hpi), snap-frozen in liquid nitrogen, and stored at −80°C for RNA extraction and reverse transcription quantitative PCR (RT-qPCR). All animal experiments were conducted in accordance with institutional guidelines and local legislation governing the care and use of laboratory animals. The study protocol was approved by the Institutional Animal Care and Use Committee of Ningbo University (Approval No. 12838).

Isolation of head kidney-derived MO/MΦ from large yellow croaker and *P. plecoglossicida* stimulation

Head kidney-derived MO/MΦ cells were isolated from large yellow croakers as described previously (Ren et al., 2019). Briefly, head kidney cells were isolated by Ficoll (#17544202, Cytiva, USA) density-gradient centrifugation and seeded at 2×10^7 cells/mL in medium. After overnight adhesion at 26°C in 5% CO_2, nonadherent cells were removed to obtain adherent MO/MΦ cells. Cells were challenged with live *P. plecoglossicida* at a multiplicity of infection (MOI) of 2 for gene expression analysis or an MOI of 10 for necroptosis induction; PBS-treated cells served as controls. For gene expression analysis, cells were harvested at 4, 8, 12, and 24 hpi for RT-qPCR using primers listed in Supplementary Table S1. For necroptosis assays, cells were harvested at 1, 4, 8, and 12 hpi for flow cytometry or at 1, 2, 4, and 8 hpi for western blotting.

RNA extraction and RT-qPCR

Total RNA was extracted from large yellow croaker tissues and adherent MO/MΦ cells using the RNAiso Plus Kit (#9109, TaKaRa, Japan), as described previously (Li et al., 2020a). cDNA was synthesized using AMV reverse transcriptase (#2620A, TaKaRa, Japan), and RT-qPCR was performed using Taq Pro Universal SYBR qPCR Master Mix (#Q712-02, Vazyme, China) on an ABI StepOne™ Real-Time PCR System (Applied Biosystems, USA). Relative gene expression was calculated using the $2^{-\Delta\Delta Ct}$ method, with *Lc 18S* rRNA as the reference. All reactions were performed in triplicate and independently repeated three times.

Plasmid construction and transfection

The full-length coding sequences (CDS) of *Lc*zDHHC20a, *Lc*zDHHC20b, *Lc*TRIF, and *LcRIPK3* were cloned into HA-tagged pcDNA3.1 or Flag-tagged pcDNA3.1 via seamless cloning (#CU201, TransGen, China) according to the manufacturer's instructions. Recombinant plasmids were transformed into DH5α-competent cells and verified by Sanger sequencing. Site-directed mutants were generated using a Fast Site-Directed Mutagenesis Kit (#KM101, TIANGEN, China) according to the manufacturer's instructions. Validated plasmids were transfected into HeLa or HEK293T cells using Lipofectamine 3000 (#L3000015, Thermo Fisher Scientific, USA), and the medium was replaced after 6 h for subsequent assays. All primers used are listed in Supplementary Table S1.

RNA interference

Large yellow croaker MO/MΦ cells were seeded into 6-well plates at 2×10^7 cells/well and transfected with 30 pmol *Lc*zDHHC20b siRNA or scrambled siRNA (negative control) using Lipofectamine RNAiMAX (#13778150, Thermo Fisher Scientific, USA). Cells were harvested at 24 or 48 h post-transfection to assess knockdown efficiency by RT-qPCR (Shen et al., 2020; Wu et al., 2022). To evaluate *Lc*zDHHC20b function during *P. plecoglossicida* infection, MO/MΦ cells were infected 24 h after siRNA transfection. The scrambled siRNA used in this study was a nontargeting control with no significant homology to any known large yellow croaker gene transcript. The siRNA sequences, synthesized by GenePharma (Shanghai, China), were as follows: *LczDHHC20b* siRNA 5′-AAUCUUCUCUCCUAUACUCGGdTdT-3′ (sense) and 5′-GAGUAUAGGAGAGAAGAUUGUdTdT-3′ (antisense); *LcTRIF* siRNA 5′-UCAUAGACGUCUCUUAGUCCCdTdT-3′ (sense) and 5′-GACUAAGAGACGUCUAUGACUdTdT-3′ (antisense); and scrambled siRNA: 5′-UAUUUGGUGGGUUUAAAUCUCdTdT-3′ (sense) and 5′-GAUUUAAACCCACCAAAUACAdTdT-3′ (antisense).

Immunofluorescence assays

HeLa cells were seeded in 6-well plates at 1×10^5 cells/well. After 24 h, cells were transfected with HA-tagged *Lc*zDHHC20b or Flag-tagged *Lc*TRIF plasmids using Lipofectamine 3000. At 24 h post-transfection, cells were fixed with 4% paraformaldehyde (PFA), permeabilized with 0.1% Triton X-100, and blocked. Cells were then incubated with primary antibodies at 4°C overnight and fluorophore-conjugated secondary antibodies for 1 h at room temperature (RT). Antibodies used were: anti-TOMM20 (1:500, #sc-17764, Santa Cruz Biotechnology, USA), anti-calnexin (1:500, #sc-23954, Santa Cruz Biotechnology, USA), anti-TGN38 (1:200, #sc-166594, Santa Cruz Biotechnology, USA), Alexa Fluor™ 555-conjugated secondary antibody (1:500, #A-21147, Thermo Fisher Scientific, USA), and goat anti-rabbit IgG (H+L) cross-adsorbed Alexa Fluor™ 488 secondary antibody (1:500, #A-11008, Thermo Fisher Scientific, USA). Fluorescence images were acquired using a ZEISS confocal microscope (Carl Zeiss AG, Germany) and processed with ZEN v.3.4 software.

Co-immunoprecipitation (Co-IP)

Co-IP assays were performed as described previously (He et al., 2016; Li et al., 2020b). Briefly, cells were harvested and lysed, with cleared lysates then incubated with anti-FLAG M2 affinity gel (#A2220, Sigma-Aldrich, USA) or anti-HA agarose beads (#A2095, Sigma-Aldrich, USA) for 6 h at 4°C. After washing, bound complexes were eluted in 2× sodium dodecyl sulfate-polyacrylamide gel electrophoresis (SDS-PAGE) buffer containing 5% β-mercaptoethanol, boiled at 95°C for 10 min, and analyzed by western blotting. For endogenous Co-IP, lysates were incubated with anti-TRIF antibody overnight at 4°C with rotation, followed by incubation with Protein A/G agarose beads (#20421, Thermo Fisher Scientific, USA) for 4 h. Beads were then washed, and bound complexes were collected as described above.

Western blotting

Western blotting was conducted as described previously (Nie et al., 2025). Briefly, cells were lysed in prechilled RIPA lysis buffer (#89901, Thermo Fisher Scientific, USA) supplemented with protease inhibitor cocktail (#A32965, Thermo Fisher Scientific, USA), rotated for 20 min at 4°C, and centrifuged at

12 000 ×*g* at 4°C for 10 min. Protein concentrations were quantified by BCA assay. Samples were separated by 10% SDS-PAGE, transferred to polyvinylidene fluoride (PVDF) membranes (ISEQ00010, Millipore, Germany), blocked with 5% nonfat milk, and probed with primary antibodies overnight at 4°C. After washing with TBST, membranes were incubated with horseradish peroxidase (HRP)-conjugated secondary antibodies for 1 h at room temperature, followed by enhanced chemiluminescence (ECL) detection (#32106, Thermo Fisher Scientific, USA; #WBKLS0500, Millipore, Germany). Antibodies used were: Necroptosis Antibody Sampler Kit (1:1 000, #98110, CST, USA), GAPDH mAb (1:5 000, #M20006, Abmart, China), anti-β-tubulin (1:4 000, #M20005, Abmart, China), mouse anti-HA (1:4 000, #M20003, Abmart, China), rabbit anti-HA (1:4 000, #TT0050, Abmart, China), rabbit anti-FLAG tag (1:3 000, #TT0053, Abmart, China), mouse anti-FLAG tag (1:3 000, #M20008, Abmart, China), HRP-conjugated goat anti-rabbit IgG (1:3 000, #M21002, Abmart, China), and HRP-conjugated goat anti-mouse IgG (1:3 000, #M21001, Abmart, China).

Bactericidal assay

Bactericidal assays were performed as described previously (Nie et al., 2019; Ning et al., 2018). Large yellow croaker MO/MΦ cells were seeded in 6-well plates at 2×10^6 cells per well. Cells were infected with *P. plecoglossicida* at an MOI of 2 for 30 min. After treatment with gentamicin (0.05 mg/mL, #1405-41-0, MACKLIN, China), cells were divided into two groups. For the uptake group, cells were lysed immediately with 1% Triton X-100 to quantify phagocytosis. For the killing group, cells were incubated for 1.5 h at 28°C before lysis to assess intracellular bacterial killing. Lysates were centrifuged at 12 000 ×*g* at RT for 10 min, and the resulting supernatants were plated on Luria-Bertani (LB) agar. Colony counts were used to quantify phagocytic and bactericidal efficiency.

Flow cytometry

Large yellow croaker MO/MΦ cells were transfected with either siRNA targeting *Lc*zDHHC20b or scrambled siRNA for 24 h, followed by infection with *P. plecoglossicida* at an MOI of 10 to induce necroptosis. Cells were collected at 1, 4, 8, and 12 hpi and stained using a FITC Annexin V Apoptosis Detection Kit I (#556574, BD Pharmingen, USA) according to the manufacturer's instructions. Apoptotic and necrotic cell populations were quantified by flow cytometry using a MACSQuant Analyzer 10 (Miltenyi Biotec, Germany), and data were analyzed with MACSQuant analysis software (Miltenyi Biotec, Germany).

Acyl-biotin exchange (ABE) assay

ABE assays were performed as established in previous studies (Mateo-Tórtola et al., 2023; Nie et al., 2025). Briefly, cell lysates were centrifuged at 12 000 × *g* at 4°C for 10 min, and clarified supernatants were collected and blocked with MMTS (#208795, Sigma-Aldrich, USA)-containing blocking buffer. Excess MMTS was removed by chloroform/methanol precipitation. Samples were then divided and incubated with hydroxylamine (HAM, #55460, Sigma-Aldrich, USA) or HAM-free control buffer, followed by labeling with HPDP-biotin (#16459, Cayman Chemical, USA) for 1 h at RT. After precipitation, proteins were resuspended and incubated 1 h at RT with streptavidin beads to pull down palmitoylated proteins. Beads were washed with high-salt buffer and enriched palmitoylated proteins were analyzed by liquid chromatography-tandem mass spectrometry (LC-MS/MS) at PTM Biolabs Inc. (Hangzhou, China), as described previously (Dai et al., 2024), or by western blotting.

Scanning electron microscopy (SEM)

Cell samples were immediately fixed in freshly prepared fixative containing 2% paraformaldehyde and 2.5% glutaraldehyde (pH 7.0–7.2) for approximately 2 h at RT. After fixation, samples were washed three times with PBS (10 min each) and postfixed with 1% osmium tetroxide and 1.5% potassium ferrocyanide in PBS for 1 h. Samples were subsequently washed three times with PBS (10 min each) and dehydrated through a graded ethanol series of 30%, 50%, 70%, 95%, and 100%, with incubation for 15 min at each step; the 100% ethanol step was repeated twice. After dehydration, samples were subjected to critical-point drying, mounted on specimen stubs using double-sided conductive carbon tape, and sputter-coated with a 3–5 nm metal layer. Finally, specimens were observed and photographed using a scanning electron microscope (Hitachi SU8600-Quorum, Japan).

LC-MS/MS analysis

Streptavidin bead-bound proteins from the ABE assay were subjected to on-bead tryptic digestion. Trypsin was first added to a final concentration of 20 ng/μL, and samples were digested overnight. Disulfide bonds were reduced with 5 mmol/L dithiothreitol (DTT) at 37°C for 60 min, followed by alkylation with 11 mmol/L iodoacetamide (IAA) at RT in the dark for 45 min. Trypsin was subsequently added twice at a final concentration of 10 ng/μL, with digestion continued for 4 h after each addition. The resulting peptides were acidified, desalted, dissolved in solvent A (0.1% formic acid, 2% acetonitrile in water), and loaded onto a homemade reversed-phase analytical column (25 cm×100 μm inner diameter). Peptides were separated on a NanoElute UHPLC system (Bruker Daltonics) at a flow rate of 500 nL/min using the following solvent B gradient (0.1% formic acid in acetonitrile): 0–14 min, 6%–24% B; 14–16 min, 24%–35% B; 16–18 min, 35%–80% B; and 18–20 min, 80% B. Peptides were analyzed on a timsTOF Pro Mass Spectrometer (Bruker Daltonics, USA) in dia-PASEF mode with a capillary electrospray voltage of 1.75 kV. Full MS scans were acquired over m/z 300–1 500, with 20 PASEF-MS/MS scans per cycle. The MS/MS scan range was m/z 400–8 500, and the isolation window was 7 m/z.

Raw DIA data were processed using DIA-NN v.1.8. Trypsin/P was specified as the cleavage enzyme, with up to one missed cleavage allowed. N-terminal methionine excision and cysteine carbamidomethylation were set as fixed modifications. The false discovery rate (FDR) was controlled at <1%. Functional enrichment analysis of differentially palmitoylated proteins was performed using Gene Ontology (GO) and Kyoto Encyclopedia of Genes and Genomes (KEGG) pathway annotations. GO IDs were assigned using eggNOG-mapper, and proteins were classified into biological process, cellular component, and molecular function categories. KEGG annotation was performed by BLAST search against the KEGG database (e-value ≤$1e^{-4}$). Significantly enriched terms were identified using Fisher's exact test and defined by fold enrichment>1.5 and P<0.05. Differentially palmitoylated proteins were defined by absolute $\log_2$(fold change)≥1, corresponding to at least a 2-fold alteration in protein abundance, in conjunction with an FDR-adjusted P<0.05.

Statistical analysis

Data are presented as mean±standard error of the mean (SEM), and each experiment was independently repeated at least three times. Statistical analyses were performed using GraphPad Prism v.8. Comparisons between two groups were conducted using unpaired Student's *t*-tests. $^{*}P<0.05$ and $^{**}P<0.01$ were considered statistically significant.

RESULTS

Large yellow croaker contains two zDHHC20 isoforms

Genome annotation identified two zDHHC20 paralogs in large yellow croaker, designated *Lc*zDHHC20a and *Lc*zDHHC20b, on chromosomes X and XXIII, respectively. Genomic synteny analysis supported their paralogous relationship and indicated divergent evolutionary trajectories after duplication (Dai et al., 2024). The *Lc*zDHHC20a locus exhibited conserved synteny with zDHHC20a loci in *Fundulus heteroclitus* and *Danio rerio*, including shared flanking genes such as *phldb2a* and *gabrr3a*. In contrast, *Lc*zDHHC20b showed conserved synteny with the zDHHC20 locus in *Epinephelus lanceolatus* and the zDHHC20b locus in *Danio rerio*, with retention of flanking genes such as *slc51a* and *pdk3* (Figure 1A). The human zDHHC20 locus displayed a different genomic context, consistent with lineage-specific chromosomal rearrangement after duplication. These results indicate that *Lc*zDHHC20a and *Lc*zDHHC20b represent two teleost zDHHC20 paralogs that likely originated through teleost-specific genome duplication and subsequently retained distinct genomic contexts.

Phylogenetic analysis further resolved the evolutionary separation of these two genes. zDHHC20 amino acid sequences from representative teleosts and other vertebrates divided teleost proteins into two major lineages corresponding to zDHHC20a- and zDHHC20b-related clades, whereas tetrapod sequences formed a single-copy zDHHC20 lineage (Figure 1B). Within this framework, *Lc*zDHHC20a grouped with teleost zDHHC20a homologs, whereas *Lc*zDHHC20b clustered within the teleost zDHHC20b-related lineage and was most closely related to the *Epinephelus lanceolatus* ortholog. These results support the existence of two evolutionarily distinct zDHHC20 isoforms in large yellow croaker. To further examine their relatedness, amino acid sequence comparisons were performed among representative vertebrate homologs. *Lc*zDHHC20a shared 68.16%, 70.20%, 64.35%, 63.82%, 61.19%, and 59.49% similarity with *El*zDHHC20, *Dr*zDHHC20a, *Xl*zDHHC20, *Cm*zDHHC20, *Hs*zDHHC20, and *Mm*zDHHC20, respectively. In contrast, *Lc*zDHHC20b exhibited markedly higher similarity to the same homologs, reaching 94.93%, 86.67%, 75.43%, 77.87%, 72.14%, and 71.31%, respectively. These values indicate that *Lc*zDHHC20b is substantially more conserved than *Lc*zDHHC20a, particularly in relation to teleost and mammalian zDHHC20 orthologs. Multiple sequence alignment further demonstrated that both *Lc*zDHHC20a and *Lc*zDHHC20b retained the highly conserved DHHC catalytic motif (Asp-His-His-Cys) and major hydrophobic regions characteristic of zDHHC palmitoyltransferases (Figure 1C). However, *Lc*zDHHC20b exhibited broader conservation across the full protein, with an architecture more closely resembling zebrafish zDHHC20b and *Xenopus*, turtle, human, and mouse zDHHC20 proteins, whereas *Lc*zDHHC20a displayed greater divergence.

Structural modeling using AlphaFold 3 further supported this distinction (Figure 1D). *Lc*zDHHC20b exhibited the typical four-transmembrane-domain topology observed in most vertebrate zDHHC20 proteins, including zebrafish, human, mouse, tropical clawed frog, and green sea turtle homologs. In contrast, *Lc*zDHHC20a was predicted to contain five transmembrane domains, indicating a noncanonical topology relative to *Lc*zDHHC20b and most vertebrate homologs. This structural difference suggests post-duplication divergence between the two paralogs, with *Lc*zDHHC20b retaining the conserved zDHHC20 architecture and *Lc*zDHHC20a potentially undergoing functional specialization. Collectively, these findings show that large yellow croaker encodes two evolutionarily and structurally distinct zDHHC20 isoforms, with *Lc*zDHHC20b representing the paralog most similar to canonical vertebrate zDHHC20 proteins.

***Lc*zDHHC20b is the infection-responsive zDHHC20 paralog in large yellow croaker**

To determine the zDHHC20 paralog most closely associated with antibacterial immunity, transcript dynamics of *Lc*zDHHC20a and *Lc*zDHHC20b were compared in large yellow croaker after *P. plecoglossicida* infection. Under bacterial challenge, *Lc*zDHHC20a exhibited only limited infection responsiveness. Modest induction was observed in several tissues, including the intestine, liver, and trunk kidney, but these changes were weak and inconsistent across the infection time course (Supplementary Figure S1A–F). In primary head kidney-derived MO/MΦ, *Lc*zDHHC20a remained largely unchanged after bacterial stimulation (Supplementary Figure S1G), indicating that this paralog is unlikely to play a major role in the MO/MΦ response to *P. plecoglossicida*. In contrast, *Lc*zDHHC20b displayed a broader and more robust infection-induced expression profile. Following *P. plecoglossicida* challenge, *Lc*zDHHC20b exhibited marked tissue-specific and time-dependent regulation. In the gill and spleen, transcript levels increased sharply, peaking at 6 and 48 hpi, respectively, before returning to baseline or lower levels (Supplementary Figure S2A, B). In the trunk kidney, head kidney, intestine, and liver, *Lc*zDHHC20b was persistently up-regulated, with tissue-specific peaks during early or intermediate infection and sustained elevation throughout the 72 h observation period (Supplementary Figure S2C–F). Previous profiling of the zDHHC family in primary MO/MΦ cells also identified *Lc*zDHHC20b as an infection-responsive family member during *P. plecoglossicida* challenge (Dai et al., 2024). Together, these expression patterns indicate that *Lc*zDHHC20b, rather than *Lc*zDHHC20a, is the zDHHC20 paralog more strongly associated with the antibacterial response, particularly in MO/MΦ. Subsequent functional analyses therefore focused on the role of *Lc*zDHHC20b.

siRNA-mediated knockdown was then applied to confirm the role of *Lc*zDHHC20b in MO/MΦ immune responses. RT-qPCR confirmed efficient silencing, with *Lc*zDHHC20b transcript levels reduced by 99.0% and 96.0% at 24 and 48 h post-transfection, respectively, compared with scrambled siRNA controls (Figure 2A). Following *P. plecoglossicida* infection, *Lc*zDHHC20b-deficient MO/MΦ cells displayed a pronounced shift in inflammatory signaling. The proinflammatory cytokines IL-1β, IL-6, and TNF-α were significantly up-regulated, with peak induction occurring between 4 and 12 hpi (Figure 2B–D). Conversely, the anti-inflammatory cytokines IL-10 and TGF-β were markedly reduced, particularly during the intermediate stage of infection (8–12 hpi) (Figure 2E, F). These findings indicate that *Lc*zDHHC20b restrains inflammatory activation in infected MO/MΦ and that its depletion skews these cells

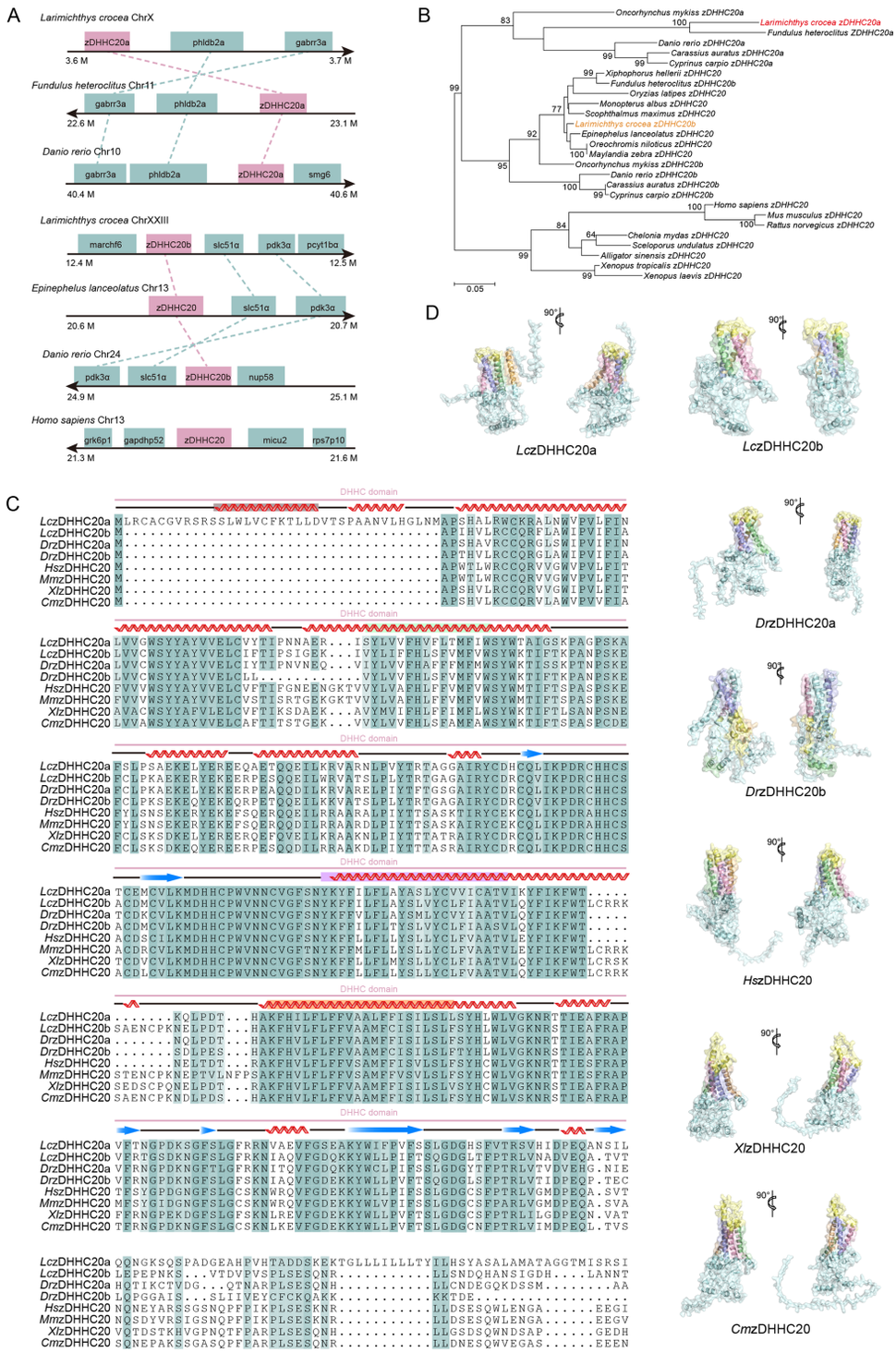

Figure 1 Bioinformatics analysis of *Lcz*DHHC20a and *Lcz*DHHC20b

A: Gene synteny and chromosomal localization of the two zDHHC20 paralogs in *Larimichthys crocea* and homologous loci in representative teleost and mammalian species. Conserved neighboring genes and transcriptional orientations are indicated. B: Phylogenetic relationships among zDHHC20 homologs from representative teleosts and other vertebrates. The tree was constructed based on amino acid sequences. Multiple sequence alignment was performed using Clustal Omega in MEGA 12, and the best amino acid substitution model was selected according to the lowest Bayesian Information Criterion (BIC) value using the “Find Best Protein Model (ML)” function. A maximum-likelihood phylogenetic tree was then generated using the selected model with 1 000 bootstrap replicates and the subtree-pruning-regrafting (SPR) heuristic search method. The tree was rooted with tetrapod zDHHC20 sequences. Bootstrap support values (>60) are shown at the corresponding nodes, and branch lengths are indicated. C: Multiple sequence alignment of zDHHC20 proteins from representative species. Conserved residues are shaded in dark gray (identical) and light gray (similar). The conserved DHHC domain is indicated above the alignment. Secondary structural elements are shown above the sequences, with red coils representing α-helices and blue arrows indicating β-sheets. D: Predicted tertiary structures of *Lcz*DHHC20a, *Lcz*DHHC20b, *Drz*DHHC20a, *Drz*DHHC20b, *Hsz*DHHC20, *Xlz*DHHC20, and *Cmz*DHHC20 generated by AlphaFold 3. Conserved features of the DHHC domain are highlighted and aligned for structural comparison. Full species names corresponding to abbreviations are provided in Supplementary Table S2.

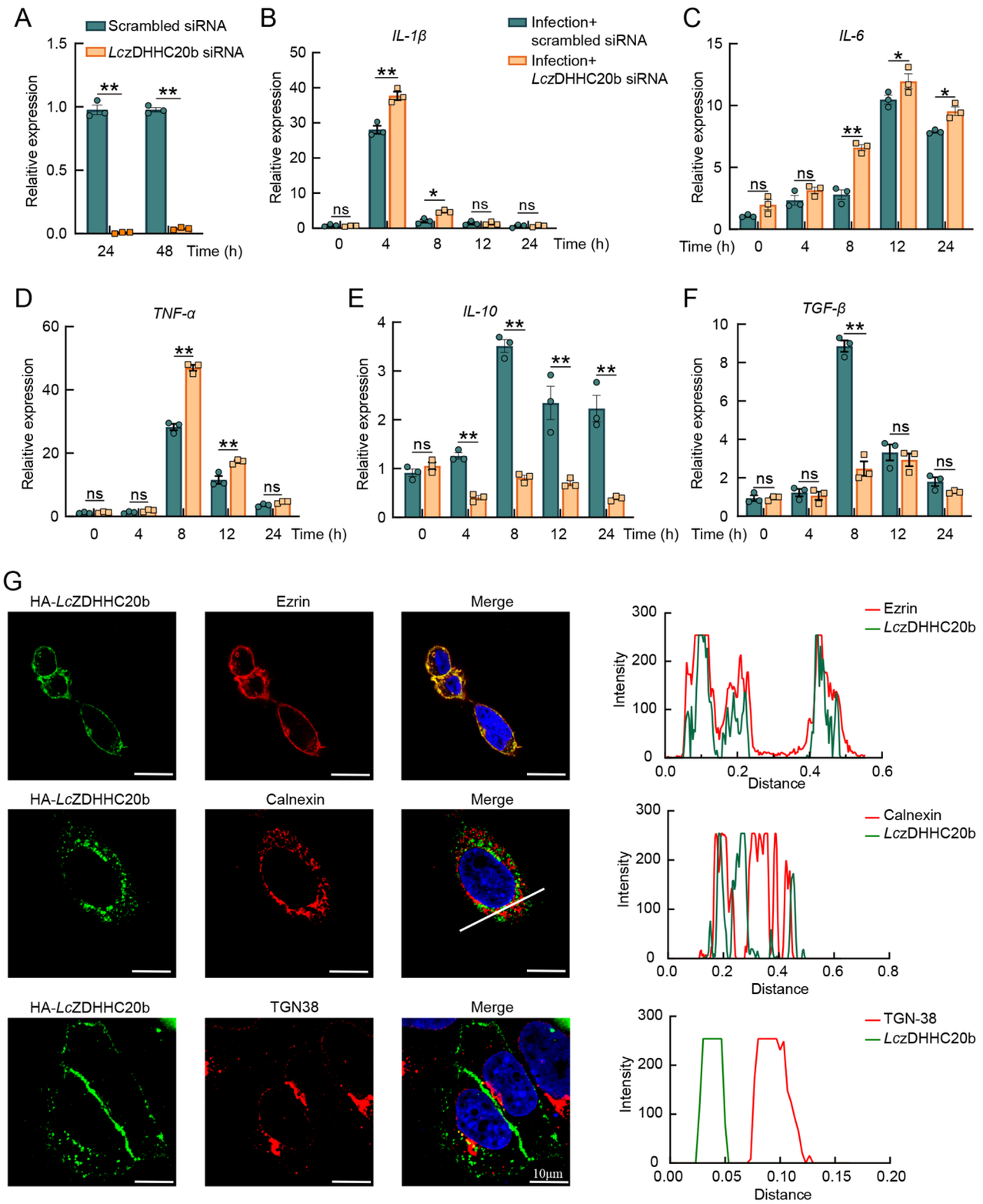

Figure 2 Subcellular localization and immunoregulatory function of *Lcz*DHHC20b in *Pseudomonas plecoglossicida*-infected MO/MΦ

A: Knockdown efficiency of *Lcz*DHHC20b siRNA was quantitatively assessed by qRT-PCR analysis. Relative mRNA expression levels were calculated using the $2^{-\Delta\Delta CT}$ method, with *18S rRNA* as the internal reference, and normalized to scrambled siRNA-treated controls at 24 hours post transfection. B–F: Expression profiles of cytokine genes (*IL-1β*, *IL-6*, *IL-10*, *TGF-β*, and *TNF-α*) in MO/MΦ after *Lcz*DHHC20b knockdown and *P. plecoglossicida* infection (MOI=2). Cells were harvested at indicated time points, and mRNA levels were quantified by RT-qPCR using the $2^{-\Delta\Delta CT}$ method, with *18S rRNA* as the endogenous control and normalization to the 0 h baseline. Data are presented as mean±SEM (n=3). *: P<0.05; **: P<0.01; ns: Not significant. G: Immunofluorescence analysis of HA-tagged *Lcz*DHHC20b localization in HeLa cells. Cells were co-stained with markers for the plasma membrane (Ezrin), endoplasmic reticulum (Calnexin), and trans-Golgi network (TGN38). Fluorescence intensity profiles, represented by green and red curves, were quantitatively analyzed using ZEN software. Scale bars: 10 μm.

toward a more proinflammatory state.

The functional relevance of this inflammatory shift was assessed using colony-forming unit (CFU) assays. Consistent with enhanced inflammatory activation, *Lc*zDHHC20b-silenced MO/MΦ cells contained significantly fewer viable intracellular bacteria than control cells, indicating increased bacterial clearance after knockdown (Supplementary Figure S3A, B). Together, these results identify *Lc*zDHHC20b as an infection-responsive immune regulator that restrains inflammatory output and modulates antibacterial activity in teleost macrophages during *P. plecoglossicida* infection.

Subcellular localization was examined to further characterize *Lc*zDHHC20b. zDHHC family members are typically localized to the endoplasmic reticulum (ER), Golgi apparatus, and/or cytoplasmic membrane (Philippe & Jenkins, 2019). Immunofluorescence analysis of HEK293T cells expressing HA-tagged *Lc*zDHHC20b revealed strong colocalization with Ezrin, a plasma membrane-associated marker, but little or no colocalization with Calnexin, an ER marker, or TGN38, a trans-Golgi network marker, indicating that *Lc*zDHHC20b predominantly localizes to the cytoplasmic membrane (Figure 2G). This distribution partially resembles that reported for mammalian zDHHC20 (Draper & Smith, 2010), supporting the classification of *Lc*zDHHC20b as the canonical zDHHC20 paralog in large yellow croaker and suggesting a role in palmitoylation-dependent regulation of immune signaling at membrane-associated sites.

*Lc*zDHHC20b promotes necroptosis in MO/MΦ during *P. plecoglossicida* infection

Given the established role of *Lc*zDHHC20b in inhibiting inflammatory responses, its potential involvement in infection-induced MO/MΦ death was next examined. Flow cytometry using Annexin V and propidium iodide (PI) staining showed that high-dose *P. plecoglossicida* infection (MOI=10) induced prominent necroptotic cell death in control MO/MΦ cells, with Annexin V^+/PI^+ cells reaching 70.63%±4.85% at 12 hpi (Figure 3A). *Lc*zDHHC20b knockdown markedly reduced this population to 52.73%±4.10% at the same time point (Figure 3A). In contrast, apoptotic cell proportions did not differ significantly between *Lc*zDHHC20b-silenced and control cells, indicating that *Lc*zDHHC20b selectively promotes the necroptotic response rather than broadly increasing cell death (Supplementary Figure S4A).

Consistent with the flow cytometry data, biochemical analysis of key necroptosis-associated signaling revealed infection-induced activation of the RIPK3-MLKL pathway. Phosphorylated RIPK3 (p-RIPK3), RIPK1 (p-RIPK1), and MLKL (p-MLKL) increased in a time-dependent manner post-infection, with stronger activation at later time points (Figure 3B; Supplementary Figure S4B). *Lc*zDHHC20b silencing substantially attenuated the infection-induced phosphorylation of RIPK3 and MLKL, whereas p-RIPK1 showed only a modest decrease. Total RIPK1, RIPK3, and MLKL protein levels remained largely unchanged (Figure 3B; Supplementary Figure S4B), further supporting a role for *Lc*zDHHC20b as a positive regulator of necroptosis. These results indicate that *Lc*zDHHC20b facilitates necroptotic signaling primarily through activation of the RIPK3-MLKL arm.

SEM was then used to assess morphological features of this cell death phenotype. At 8 hpi, control MO/MΦ cells transfected with scrambled siRNA exhibited extensive membrane injury, including a roughened and collapsed cell surface, abundant vesicle-like protrusions, structural disintegration, and apparent leakage of intracellular contents (Figure 3C). By 12 hpi, these cells exhibited more advanced destruction, with extensive structural collapse, large membrane perforations, and a hollowed morphology indicative of terminal membrane rupture (Figure 3C). In contrast, *Lc*zDHHC20b-silenced cells retained a more intact overall structure at 8 hpi, with only limited membrane damage and small surface perforations. At 12 hpi, *Lc*zDHHC20b-deficient cells showed more pronounced swelling and bubble-like protrusions, indicating progression toward lytic death, but still lacked the extensive rupture and large-scale structural collapse observed in control cells (Figure 3C). Together, the flow cytometric, biochemical, and ultrastructural data demonstrate that *Lc*zDHHC20b promotes infection-induced necroptotic cell death in teleost macrophages.

*Lc*zDHHC20b facilitates necroptosis by promoting TRIF palmitoylation

To determine whether *Lc*zDHHC20b promotes necroptosis through palmitoylation-dependent control of immune signaling proteins, ABE enrichment was coupled with LC-MS/MS to profile the palmitoylated proteome of *P. plecoglossicida*-infected MO/MΦ. Cells were transfected with either scrambled siRNA (siCon) or *Lc*zDHHC20b-specific siRNA (siZD20b) and infected with *P. plecoglossicida* for 8 h before ABE enrichment and LC-MS/MS analysis (Figure 4A). HAM-untreated samples were included as negative controls to eliminate nonspecific biotinylation or bead-associated background (Figure 4A). The proteomic dataset was deposited in the ProteomeXchange Consortium via the PRIDE partner repository under accession number PXD065712.

LC-MS/MS analysis identified extensive protein palmitoylation in both infected control and *Lc*zDHHC20b-silenced MO/MΦ. In total, 4 233 palmitoylated proteins were detected in the siCon_HAM group, whereas 4 171 were detected in the siZD20b_HAM group, with 3 889 proteins shared between the two groups (Figure 4B). In addition, 344 proteins were identified only in control cells, whereas 282 proteins were specific to the *Lc*zDHHC20b-silenced cells (Figure 4B). These data indicate that loss of *Lc*zDHHC20b significantly reshapes the palmitoylation landscape of infected MO/MΦ during *P. plecoglossicida* infection.

Functional annotation was then performed to define the cellular distribution and biological features of the identified palmitoylated proteins. In the siCon_HAM group, 3 447 proteins were annotated in the COG/KOG database, 2 548 in the domain database, 2 143 in the KEGG database, and 3 409 by GO analysis (Supplementary Figure S5A). Subcellular localization analysis assigned 1 586 proteins to the cytoplasm, 939 to the nucleus, 517 to the plasma membrane, and 464 to the mitochondria (Supplementary Figure S5B). GO classification distributed these proteins across biological process, cellular component, and molecular function categories (Supplementary Figure S5C–E). In the siZD20b_HAM group, 3 931 proteins were annotated in the COG/KOG database, 2 884 in the domain database, 4 100 in the KEGG database, and 3 917 by GO analysis (Supplementary Figure S6A). Subcellular localization profiling identified 1 760 cytoplasmic, 1 046 nuclear, 704 plasma membrane-associated, and 522 mitochondrial proteins (Supplementary Figure S6B), with GO classification again spanning biological process, cellular component, and molecular function categories (Supplementary Figure S6C–E). Thus, the two groups showed broadly comparable annotation

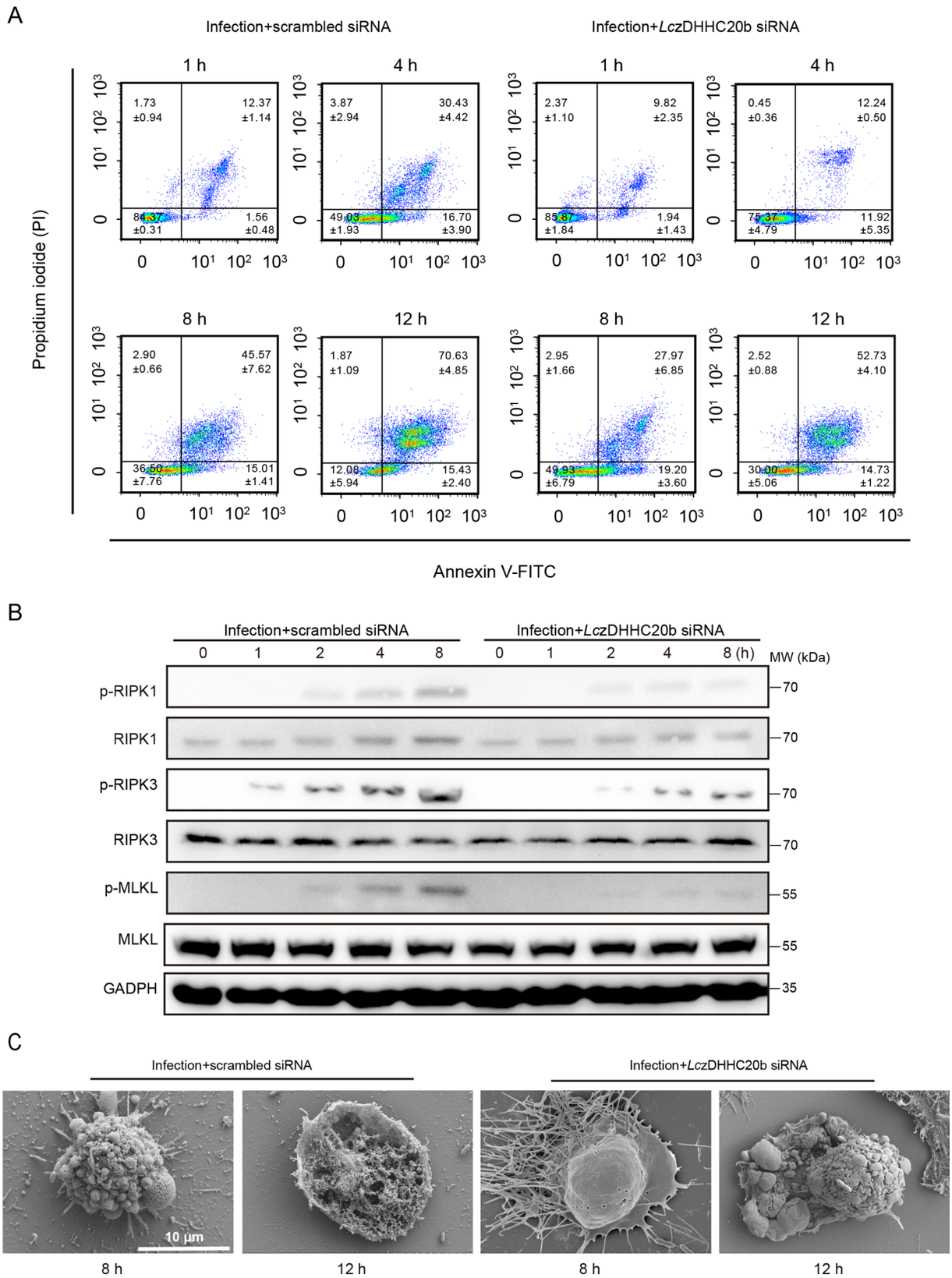

Figure 3 *Lcz*DHHC20b deficiency attenuates *Pseudomonas plecoglossicida*-induced necroptotic cell death in MO/MΦ

A: Flow cytometric analysis of cell death in MO/MΦ cells transfected with scrambled or *Lcz*DHHC20b siRNA for 24 h prior to infection with *P. plecoglossicida* at an MOI of 10. At 1, 4, 8, and 12 hpi, cells were stained with Annexin V-FITC and propidium iodide (PI). Cell populations were classified as live (Annexin V^-/PI^-), early apoptotic (Annexin V^+/PI^-), necroptotic (Annexin V^+/PI^+), or dead (Annexin V^-/PI^+). B: Western blot analysis of necroptosis-related signaling proteins. Lysates from the same experimental groups were probed for phosphorylated and total RIPK1, RIPK3, and MLKL. GAPDH was used as the loading control. C: Scanning electron microscopy (SEM) of infected MO/MΦ morphology in scrambled siRNA and *Lcz*DHHC20b siRNA groups at 8 and 12 hpi. Representative images show progressive membrane damage and structural disruption in control cells, whereas *Lcz*DHHC20b-silenced cells display relatively preserved morphology and reduced membrane rupture. Scale bars: 10 μm.

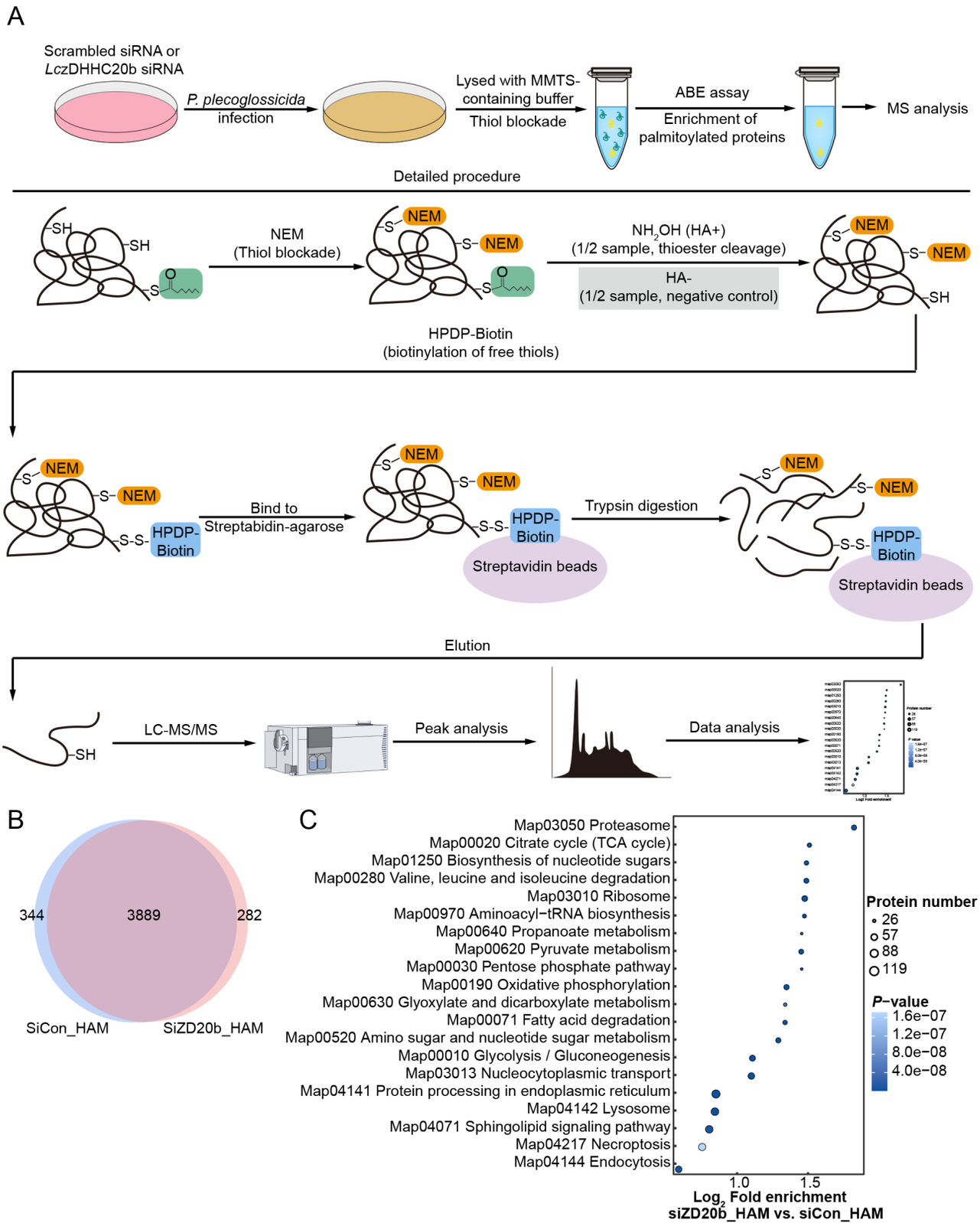

Figure 4 Palmitoylated proteome profiling in *Pseudomonas plecoglossicida*-infected MO/MΦ following *Lc*zDHHC20b knockdown

A: Schematic overview of the acyl-biotin exchange (ABE) workflow coupled with LC-MS/MS for identifying palmitoylated proteins in large yellow croaker MO/MΦ. Cells were transfected with scrambled or *Lc*zDHHC20b siRNA and infected with *P. plecoglossicida*. Proteins were subjected to thiol blockade, hydroxylamine (HAM)-dependent cleavage of thioester bonds, biotinylation of free thiols, affinity purification with streptavidin-agarose beads, and LC-MS/MS analysis. B: Venn diagram showing overlapping and unique palmitoylated proteins identified in control (siCon_HAM) and *Lc*zDHHC20b-silenced (siZD20b_HAM) groups following HAM treatment. C: Bubble plot showing the top 20 enriched KEGG pathways in siZD20b_HAM versus siCon_HAM groups. Y-axis denotes KEGG pathway categories, while x-axis represents $\log_2$-transformed enrichment scores. Bubble size represents number of proteins mapped to each pathway, and color intensity reflects statistical significance, with darker blue denoting smaller *P*-values.

profiles, but *Lc*zDHHC20b knockdown was associated with subtle shifts in both subcellular enrichment and functional composition of the palmitoylated proteome.

Pathway enrichment analysis comparing siZD20b_HAM with siCon_HAM groups identified necroptosis as one of the most significantly affected pathways (Figure 4C), linking *Lc*zDHHC20b-dependent palmitoylation to the cell death phenotype observed during infection. Proteins associated with apoptosis and necroptosis were markedly up-regulated in the siZD20b_HAM group relative to the siCon_HAM group (Figure 5A), with several key regulatory factors exhibiting distinct fold-change patterns (Figure 5B). Among these candidates, TIR-domain-containing adapter-inducing interferon-β (TRIF) showed the most significant decrease in palmitoylated form in the *Lc*zDHHC20b knockdown group, with the TRIF protein not detected in the siZD20b_HAM group. Given that TRIF functions as a TLR adaptor capable of recruiting RIPK3 through RIP homotypic interaction motif (RHIM)-mediated interactions, loss of TRIF palmitoylation suggests that *Lc*zDHHC20b may act upstream of necrosome assembly.

ABE validation confirmed that *Lc*TRIF is palmitoylated. In HEK293T cells overexpressing Flag-tagged *Lc*TRIF, TRIF underwent palmitoylation in a hydroxylamine-dependent manner, consistent with S-palmitoylation (Figure 5C). Moreover, palmitoylated TRIF abundance was significantly lower in siZD20b_HAM cells than in control cells (Figure 5D), indicating that *Lc*zDHHC20b is required for TRIF palmitoylation. To further identify the palmitoylation site(s) of *Lc*TRIF, five candidate cysteine residues (Cys92, Cys142, Cys158, Cys397, and Cys545) were predicted using GPS-Palm and individually substituted with alanine. Mutation of Cys92 (C92A) or Cys142 (C142A) markedly weakened the *Lc*TRIF palmitoylation signal, whereas mutation of Cys158 (C158A), Cys397 (C397A), or Cys545 (C545A) produced only limited effects (Figure 5E). These results suggest that Cys92 and Cys142 are major residues contributing to *Lc*TRIF palmitoylation. Multiple sequence alignment further showed that both cysteines were well conserved among several teleost TRIF homologs, but were not broadly conserved in the mammalian, amphibian, or reptilian sequences examined (Figure 5F), suggesting a teleost-enriched regulatory feature.

The effect of palmitoylation on *Lc*TRIF subcellular distribution was then examined by immunofluorescence. Wild-type *Lc*TRIF showed detectable colocalization with Calnexin and TGN38, indicating association with ER and trans-Golgi network compartments (Figure 5G). In contrast, the palmitoylation-deficient C92/142A mutant lost these clear colocalization signals, suggesting that palmitoylation supports normal *Lc*TRIF trafficking or compartmental association. Neither wild-type *Lc*TRIF nor the C92/142A mutant showed clear colocalization with TOMM20 under the conditions tested (Figure 5G).

Together, these results identify TRIF as a novel palmitoylation substrate regulated by *Lc*zDHHC20b and define Cys92 and Cys142 as major residues contributing to this modification. TRIF palmitoylation appears to support association with ER and trans-Golgi network compartments, providing a spatial framework for TRIF-dependent signaling. The data also support a functional link between *Lc*zDHHC20b-mediated TRIF palmitoylation and activation of necroptosis during *P. plecoglossicida* infection and reveal a lipid-based mechanism through which *Lc*zDHHC20b promotes inflammatory cell death in teleost macrophages.

*Lc*TRIF promotes *P. plecoglossicida*-induced MO/MΦ necroptosis through interaction with *Lc*RIPK3

The functional contribution of *Lc*TRIF to infection-induced necroptosis was examined by siRNA-mediated knockdown in large yellow croaker MO/MΦ. RT-qPCR confirmed efficient silencing, with *Lc*TRIF mRNA levels reduced to approximately 3% and 14% of control levels at 24 and 48 h post-transfection, respectively (Supplementary Figure S7A). Flow cytometry analysis revealed that after *P. plecoglossicida* infection, *Lc*TRIF knockdown markedly reduced the Annexin V^+/PI^+ necroptotic population at 12 hpi, from 74.03%±2.67% in scrambled siRNA-transfected cells to 51.33%±7.97% in *Lc*TRIF-deficient cells (Figure 6A; Supplementary Figure S7B). SEM provided morphological support for this protective effect. Control cells showed extensive membrane deformation and abundant vesicle-like protrusions by 8 hpi, followed by severe rupture, surface collapse, fragmentation, and apparent leakage of intracellular contents by 12 hpi (Figure 6B). In contrast, *Lc*TRIF-silenced cells retained a more continuous cell surface at 8 hpi, despite visible wrinkling and membrane irregularity. Even at 12 hpi, these cells showed compact swelling, coarse surface folds, and limited protrusive damage but lacked the extensive rupture and leakage observed in control cells (Figure 6B). These observations indicate that *Lc*TRIF knockdown markedly attenuates infection-induced lytic membrane damage, consistent with reduced necroptotic progression.

To validate the role of *Lc*TRIF in necroptotic signaling, activation of key necroptosis markers, including p-RIPK1, p-RIPK3, and p-MLKL, was assessed. Western blot analysis revealed a time-dependent increase in phosphorylation levels post-infection, with stronger activation at later stages. In contrast, *Lc*TRIF knockdown markedly suppressed p-RIPK3 and p-MLKL but exerted only a modest effect on p-RIPK1 levels. Notably, total RIPK1, RIPK3, and MLKL protein levels remained largely unchanged (Figure 6C; Supplementary Figure S7C), suggesting that *Lc*TRIF primarily affected phosphorylation-dependent pathway activation rather than expression of core necroptotic proteins. These findings indicate that *Lc*TRIF acts as a positive regulator of *P. plecoglossicida*-induced necroptosis, primarily by promoting RIPK3 and MLKL activation.

The persistence of RIPK1 phosphorylation during infection, together with the limited effect of *Lc*TRIF knockdown on p-RIPK1 despite markedly reducing p-RIPK3 and p-MLKL, suggested that the infection-induced necroptotic response may not be mediated exclusively through a TRIF-dependent pathway. Instead, these data support a model in which infection activates at least two converging signaling components: a TRIF-dependent branch and a RIPK1-dependent branch. To further evaluate the contribution of RIPK1, infected MO/MΦ cells were treated with the RIPK1 inhibitor Nec-1. Flow cytometry showed that Nec-1 partially reduced the Annexin V^+/PI^+ cell population during *P. plecoglossicida* infection, particularly at the later stages (Supplementary Figure S7D), indicating that RIPK1 contributes to the overall infection-induced necroptotic response but does not fully account for TRIF-dependent RIPK3-MLKL activation.

Given that mammalian TRIF can activate RIPK3 through a RIPK1-independent pathway (Zhang et al., 2024a), the interaction between *Lc*TRIF and *Lc*RIPK3 was next examined. Reciprocal Co-IP assays in HEK293T cells confirmed association between *Lc*TRIF and *Lc*RIPK3, indicating

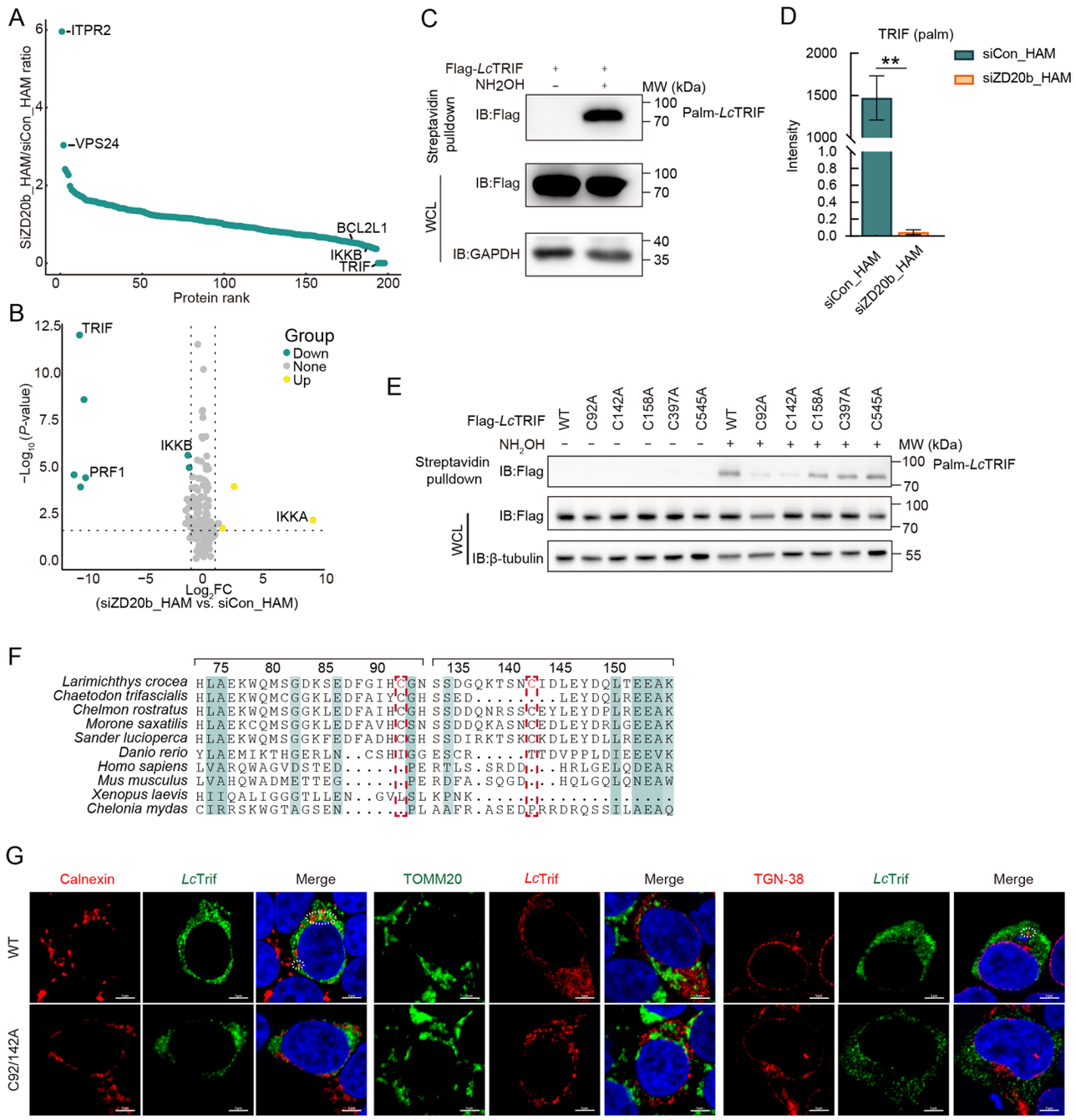

Figure 5 *Lcz*DHHC20b deficiency impairs TRIF palmitoylation in *Pseudomonas plecoglossicida*-infected MO/MΦ

A: Protein rank plot showing differentially palmitoylated proteins associated with apoptosis and necroptosis pathways in MO/MΦ transfected with *Lcz*DHHC20b siRNA (siZD20b_HAM) or scrambled control siRNA (siCon_HAM), based on LC-MS/MS quantification. B: Volcano plots showing pairwise comparisons of apoptosis- and necroptosis-related palmitoylated proteins between siZD20b_HAM and siCon_HAM groups. Vertical dashed lines indicate the $\log_2$ fold-change threshold (±1.5), and horizontal dashed line indicates statistical significance threshold ($-\log_{10}$(*P*-value)≥ 2). Green and yellow points indicate down-regulated and up-regulated proteins, respectively, and gray points denote proteins without significant differential expression. C: ABE assay showing *Lc*TRIF palmitoylation in HEK293T cells transfected with Flag-*Lc*TRIF. Samples were treated with or without hydroxylamine (NH_2OH) to cleave thioester bonds. Palmitoylated TRIF was enriched via streptavidin pulldown and detected using anti-Flag antibody. GAPDH served as the loading control. D: Quantification of palmitoylated TRIF intensity from proteomic analysis of siZD20b_HAM and siCon_HAM samples. Data are presented as mean±SEM (*n*=3); **: *P*<0.01. E: Identification of candidate *Lc*TRIF palmitoylation sites by ABE assay. Five cysteine residues predicted by GPS-Palm (Cys92, Cys142, Cys158, Cys397, and Cys545) were individually mutated to alanine and examined for effects on TRIF palmitoylation. Palmitoylated proteins were enriched by streptavidin pulldown and detected with anti-Flag antibody. β-tubulin served as the loading control. F: Multiple sequence alignment of the regions surrounding Cys92 and Cys142 in TRIF homologs from representative vertebrates. Residues corresponding to Cys92 and Cys142 in *Lc*TRIF are highlighted with red boxes. G: Immunofluorescence analysis of intracellular localization of wild-type *Lc*TRIF and the palmitoylation-deficient C92/142A mutant in HEK293T cells. Colocalization was examined using Calnexin (ER marker), TOMM20 (mitochondrial marker), and TGN38 (trans-Golgi network marker). Nuclei were stained with DAPI. White circles indicate colocalization. Scale bars: 5 μm.

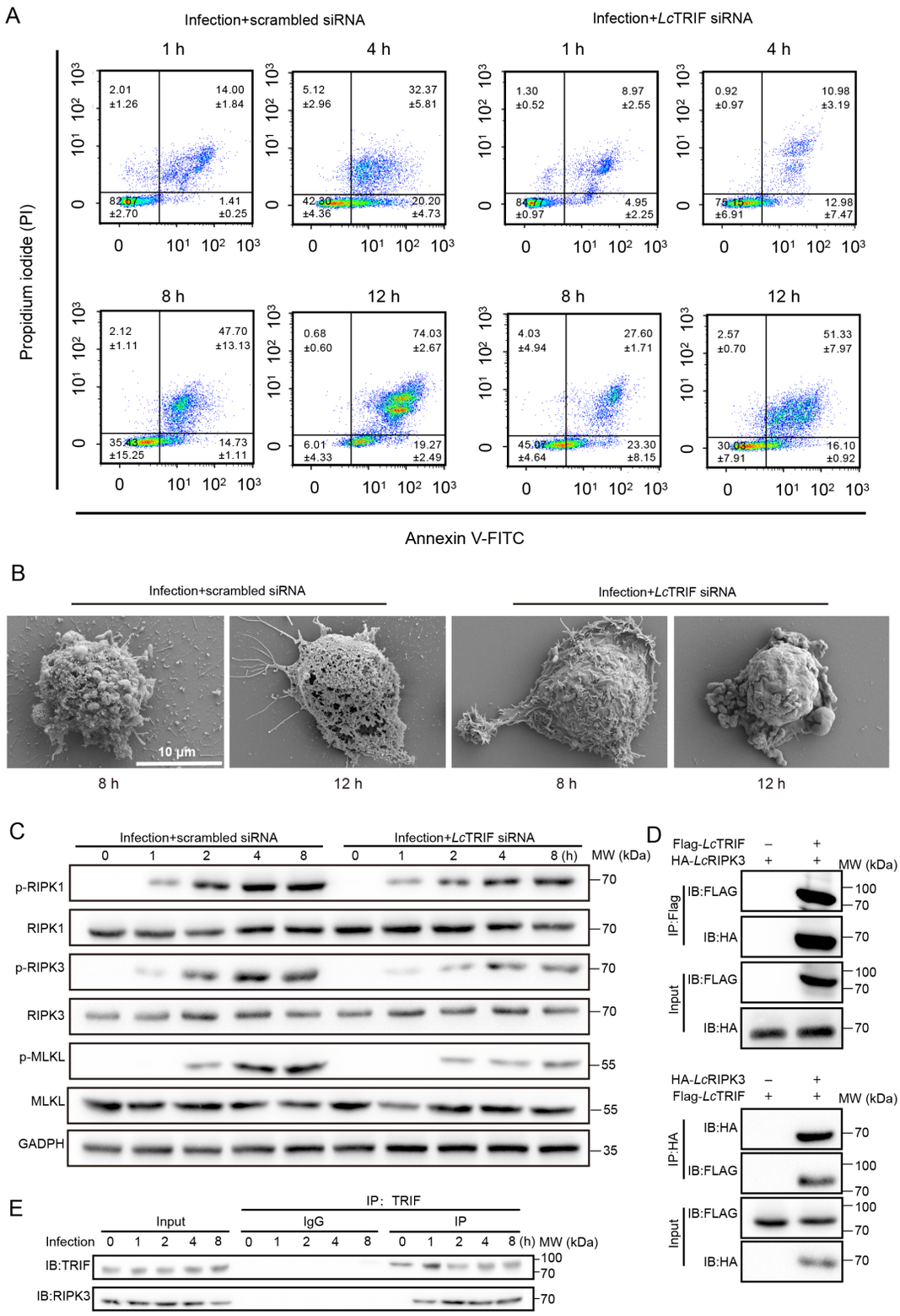

Figure 6 *Lc*TRIF promotes necroptosis through interaction with RIPK3 in *Pseudomonas plecoglossicida*-infected MO/MΦ

A: Flow cytometry analysis of cell death in MO/MΦ transfected with *Lc*TRIF siRNA or scrambled control siRNA, followed by infection with *P. plecoglossicida* (MOI=10). At 1, 4, 8, and 12 hpi, cells were stained with Annexin V-FITC and PI to discriminate between live, apoptotic, and necroptotic populations. B: SEM analysis of MO/MΦ cells transfected with *Lc*TRIF siRNA or scrambled control siRNA after *P. plecoglossicida* infection. Representative images were taken at 8 and 12 hpi. Scale bars: 10 μm. C: Western blot analysis of total and phosphorylated RIPK1, RIPK3, and MLKL in MO/MΦ cells transfected with *Lc*TRIF siRNA or scrambled control siRNA, followed by infection with *P. plecoglossicida*. Cell lysates were collected at 0, 1, 2, 4, and 8 hpi. GAPDH served as the loading control. D: Reciprocal Co-IP assays in HEK293T cells co-transfected with Flag-*Lc*TRIF and HA-*Lc*RIPK3. Protein complexes were immunoprecipitated using anti-Flag or anti-HA antibodies and immunoblotted as indicated to verify interaction between *Lc*TRIF and *Lc*RIPK3. E: Endogenous Co-IP assay detecting the interaction between native *Lc*TRIF and *Lc*RIPK3 in MO/MΦ at 0, 1, 2, 4, and 8 hpi. Immunoprecipitation was performed using anti-TRIF antibody, followed by immunoblotting with anti-RIPK3 antibody.

conservation of the TRIF-RIPK3 interaction in large yellow croaker (Figure 6D). Endogenous Co-IP in infected MO/MΦ further showed that the *Lc*TRIF-*Lc*RIPK3 complex formed rapidly after infection, becoming detectable at 1 hpi and increasing over time, with the strongest association observed at 4–8 hpi (Figure 6E). Importantly, Nec-1 treatment did not disrupt this interaction (Supplementary Figure S7E), supporting the conclusion that *Lc*TRIF-*Lc*RIPK3 complex formation is independent of RIPK1 activity. Together, these results demonstrate that *Lc*TRIF promotes *P. plecoglossicida*-induced necroptosis through interaction with *Lc*RIPK3 and activation of the RIPK3-MLKL axis, while RIPK1 provides an additional contribution to the overall necroptotic response. This TRIF-RIPK3 pathway also provides a mechanistic basis for the role of *Lc*zDHHC20b in necroptosis through regulation of *Lc*TRIF palmitoylation.

***Lc*zDHHC20b-mediated *Lc*TRIF palmitoylation promotes MO/MΦ necroptosis during *P. plecoglossicida* infection**

To explore whether *Lc*TRIF palmitoylation contributes to infection-induced necroptosis, *Lc*TRIF palmitoylation was first examined during *P. plecoglossicida* infection. ABE assays showed a progressive increase in palmitoylated *Lc*TRIF as infection advanced (Figure 7A; Supplementary Figure S8A). *Lc*zDHHC20b knockdown markedly reduced the *Lc*TRIF palmitoylation signal relative to scrambled siRNA controls (Figure 7B; Supplementary Figure S8B). Co-expression of *Lc*zDHHC20b, but not *Lc*zDHHC20a, markedly enhanced the palmitoylation signal of *Lc*TRIF (Figure 7C), further supporting *Lc*zDHHC20b as the primary zDHHC20 paralog responsible for TRIF palmitoylation in large yellow croaker. Co-IP analysis further detected an association between *Lc*zDHHC20b and *Lc*TRIF (Figure 7D), supporting a direct functional link between *Lc*zDHHC20b and *Lc*TRIF palmitoylation in MO/MΦ cells during infection.

The requirement for palmitoylation in *Lc*TRIF-*Lc*RIPK3 complex formation was then assessed. Treatment with the palmitoylation inhibitor 2-BP markedly diminished *Lc*TRIF-*Lc*RIPK3 complex formation (Figure 7E; Supplementary Figure S8C), indicating that palmitoylation facilitates or stabilizes this interaction. Consistently, endogenous Co-IP assays showed that *Lc*zDHHC20b knockdown impaired the interaction between *Lc*TRIF and *Lc*RIPK3 in infected MO/MΦ (Figure 7F; Supplementary Figure S8D). Inhibition of palmitoylation with 2-BP also substantially reduced phosphorylation of RIPK3 and MLKL, while producing only a modest effect on p-RIPK1. Total RIPK1, RIPK3, and MLKL protein levels remained largely unchanged (Figure 7G; Supplementary Figure S8E). These findings indicate that *Lc*zDHHC20b-mediated *Lc*TRIF palmitoylation is essential for efficient assembly of the *Lc*TRIF-*Lc*RIPK3 complex and subsequent activation of the downstream RIPK3-MLKL necroptotic pathway during *P. plecoglossicida* infection. This work thus uncovers palmitoylation as a previously unrecognized regulatory mechanism of TRIF-dependent necroptosis, providing novel insights into the post-translational control of innate immune signaling pathways across vertebrates.

DISCUSSION

Palmitoylation is a dynamic and reversible post-translational modification that governs protein stability, subcellular localization, and molecular complex formation (Zhang et al., 2025). This modification is catalyzed by zDHHC palmitoyltransferases and participates in diverse cellular programs, including signal transduction, membrane trafficking, and immune signaling (Tang et al., 2024; Zhou et al., 2023). Among these enzymes, zDHHC20 has drawn attention for its functions in cancer biology, particularly through the palmitoylation of oncogenic substrates such as EGFR, YTHDF3, NCAM1, and VAMP7 (Ocasio et al., 2024; Rana et al., 2018; Runkle et al., 2016; Tomić et al., 2024). In contrast, the contribution of zDHHC20 to immune regulation and pathogen-induced cell death mechanisms, such as necroptosis, remains underexplored in both mammals and nonmammalian vertebrates. The present study identified *Lc*zDHHC20b as the infection-responsive zDHHC20 paralog in large yellow croaker and demonstrated that this enzyme promotes necroptosis during *P. plecoglossicida* infection by mediating TRIF palmitoylation.

Results showed that *Lc*zDHHC20b, rather than *Lc*zDHHC20a, was closely associated with the macrophage response to *P. plecoglossicida* infection. *Lc*zDHHC20b displayed broader and stronger infection-responsive induction than *Lc*zDHHC20a across immune-relevant tissues and was previously identified as an infection-responsive zDHHC family member in primary MO/MΦ. Functionally, *Lc*zDHHC20b knockdown increased proinflammatory cytokine production while concurrently reducing anti-inflammatory cytokine expression during infection (Figure 2A–F), indicating that *Lc*zDHHC20b helps maintain inflammatory balance in infected macrophages. More importantly, *Lc*zDHHC20b knockdown markedly reduced infection-induced lytic cell death and attenuated RIPK3 and MLKL phosphorylation, establishing *Lc*zDHHC20b as a positive regulator of necroptosis in teleost macrophages (Figure 3). Comparative sequence and structural analyses showed that *Lc*zDHHC20b was more conserved than *Lc*zDHHC20a (Figure 1), whereas *Lc*zDHHC20a displayed a more divergent predicted topology and did not efficiently promote TRIF palmitoylation (Figure 7C). These findings indicate that the two paralogs are not functionally equivalent and are consistent with post-duplication divergence. The present data did not distinguish clearly between subfunctionalization, neofunctionalization, or a mixed evolutionary outcome. Nevertheless, under the infection conditions examined here, *Lc*zDHHC20b appears to retain a specialized immune-regulatory role that is not shared by *Lc*zDHHC20a.

To define the mechanism underlying this effect, ABE coupled with LC-MS/MS was used to profile the palmitoylated proteome of infected MO/MΦ after *Lc*zDHHC20b knockdown. Among the affected proteins, TRIF emerged as the most prominent necroptosis-related candidate, with a marked reduction in its palmitoylated form after *Lc*zDHHC20b depletion (Figure 5B). To the best of our knowledge, the ABE and Co-IP analyses provide the first evidence in any species that TRIF undergoes palmitoylation. Cys92 and Cys142 were identified as major residues contributing to this modification. Notably, these cysteine residues were preferentially conserved among teleost TRIF homologs, suggesting that TRIF palmitoylation may represent a lineage-enriched regulatory mechanism in fish (Figure 5E, F). TRIF palmitoylation increased during infection and depended strongly on *Lc*zDHHC20b (Figure 7A–C), linking bacterial stimulation to zDHHC20b-mediated post-translational regulation of TRIF.

*Lc*TRIF palmitoylation was necessary for efficient interaction with RIPK3, a central event in TRIF-dependent necroptotic

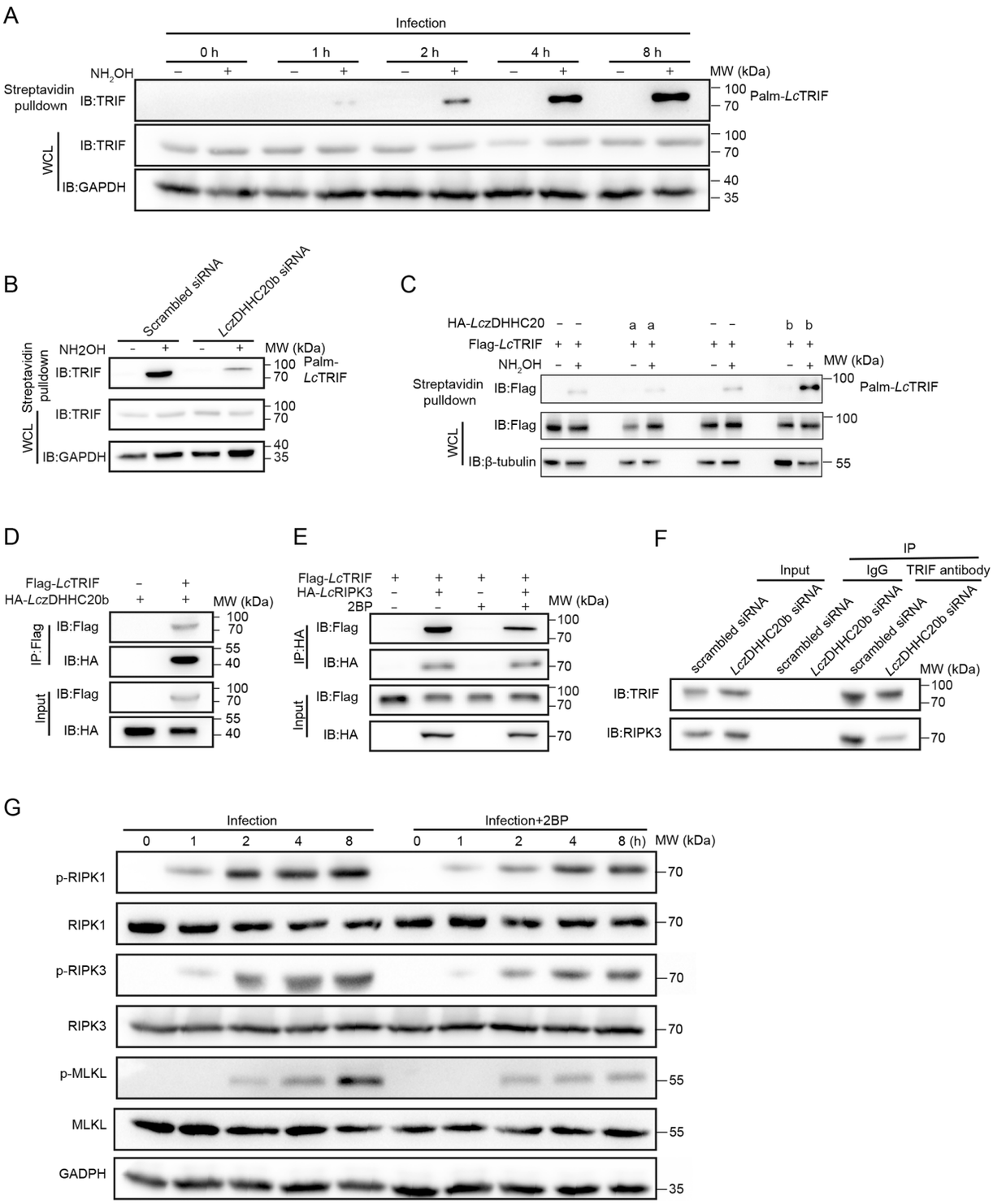

Figure 7 *Lcz*DHHC20b-mediated *Lc*TRIF palmitoylation promotes necroptosis in *Pseudomonas plecoglossicida*-infected MO/MΦ

A: Endogenous *Lc*TRIF palmitoylation in large yellow croaker MO/MΦ cells at different time points after *P. plecoglossicida* infection, assessed by ABE assay. Whole-cell lysates (WCL) were probed for TRIF, and GAPDH served as the loading control. B: ABE assay showing *Lc*TRIF palmitoylation in *P. plecoglossicida*-infected MO/MΦ cells transfected with scrambled siRNA or *Lcz*DHHC20b siRNA. GAPDH was used as the loading control. C: ABE assay assessing the effect of zDHHC20 paralog overexpression on *Lc*TRIF palmitoylation. Cells were co-transfected with Flag-*Lc*TRIF together with HA-*Lcz*DHHC20a or HA-*Lcz*DHHC20b. Palmitoylated *Lc*TRIF was enriched by streptavidin pulldown and detected with anti-Flag antibody. a and b indicate *Lcz*DHHC20a and *Lcz*DHHC20b, respectively. β-tubulin served as the loading control. D: Co-IP assay in HEK293T cells co-transfected with Flag-*Lc*TRIF and HA-*Lcz*DHHC20b to examine their interaction. Protein complexes were immunoprecipitated with anti-Flag antibody and immunoblotted with anti-HA and anti-Flag antibodies as indicated. E: Co-IP assay examining the interaction between *Lc*TRIF and *Lc*RIPK3 in the presence or absence of 2-BP, a palmitoylation inhibitor. F: Endogenous Co-IP assay detecting the interaction between *Lc*TRIF and *Lc*RIPK3 in MO/MΦ cells transfected with scrambled siRNA or *Lcz*DHHC20b siRNA after *P. plecoglossicida* infection. G: Western blot analysis of necroptosis markers (RIPK1, RIPK3, MLKL, and their phosphorylated forms) in MO/MΦ cells with or without 2-BP treatment. GAPDH served as the loading control.

signaling. Pharmacological inhibition of palmitoylation with 2-BP or zDHHC20b knockdown impaired *Lc*TRIF-*Lc*RIPK3 complex formation (Figure 7E, F), and suppressed downstream necroptotic activation, including phosphorylation of RIPK3 and MLKL (Figure 7G). Under these experimental conditions, altered TRIF palmitoylation primarily affected phosphorylation-dependent activation of the necroptotic cascade rather than the total abundance of RIPK1, RIPK3, or MLKL. However, whether this modification also influences the stability or turnover of these signaling proteins remains to be determined.

Immunofluorescence analysis further showed that wild-type *Lc*TRIF associated with ER- and trans-Golgi network-associated compartments, whereas the palmitoylation-deficient C92/142A mutant largely lost this distribution pattern (Figure 5G). These data indicate that palmitoylation at Cys92 and Cys142 is required for proper *Lc*TRIF intracellular trafficking and membrane compartmentalization. Because TRIF engages RIPK3 through RHIM, and Cys92 and Cys142 are located outside this region, palmitoylation is unlikely to constitute the direct binding interface. Instead, this modification likely facilitates the spatial organization of TRIF within signaling-competent membrane compartments that favor productive TRIF-RIPK3 complex assembly. Thus, palmitoylation may promote necroptosis by positioning TRIF in a context that supports RIPK3 recruitment and activation.

The identification of TRIF palmitoylation adds a previously unrecognized regulatory layer to the TRIF-RIPK3 axis, a pathway known to mediate RIPK1-independent necroptosis in mammals (Kaiser et al., 2013). In large yellow croaker, however, the signaling logic appears to be more complex. *Lc*TRIF knockdown strongly suppressed RIPK3 and MLKL phosphorylation but only modestly affected RIPK1 phosphorylation, indicating that TRIF primarily controls the RIPK3-MLKL branch. At the same time, pharmacological inhibition of RIPK1 partially decreased the *P. plecoglossicida*-induced Annexin V^+/PI^+ population (Supplementary Figure S7D), demonstrating that RIPK1 also contributes to the overall death response. Notably, RIPK1 inhibition did not disrupt the *Lc*TRIF-*Lc*RIPK3 interaction (Supplementary Figure S7E), indicating that assembly of the TRIF-RIPK3 complex does not require RIPK1 activity. These findings suggest that infection-induced necroptosis in large yellow croaker is not exclusively TRIF-centric but likely involves at least two convergent necroptotic routes in teleost macrophages: a RIPK1-dependent pathway and a palmitoylation-regulated TRIF-RIPK3 pathway.

This lipid-based regulation of TRIF activity expands current understanding of necroptotic signaling and may extend beyond teleosts to other species, including mammals. During bacterial infection, TRIF palmitoylation increased progressively in parallel with necroptotic cell death, suggesting that this modification forms part of an inducible host response to microbial challenge. By enhancing TRIF palmitoylation, *Lc*zDHHC20b functions as a regulatory switch that triggers macrophage necroptosis in response to infection. The biological outcome of this response is likely context dependent: regulated necroptosis may contribute to antibacterial defense or immune activation under some conditions, whereas excessive activation may amplify inflammatory tissue injury. Defining how *Lc*zDHHC20b-dependent necroptosis influences pathogen burden, tissue pathology, and immune resolution *in vivo* will be an important direction for future work.

Beyond the TRIF-RIPK3 necroptotic branch, TRIF palmitoylation may influence broader TRIF-dependent innate immune signaling. TRIF is a central adaptor downstream of TLR3 and TLR4 and links receptor activation to interferon-regulatory and inflammatory pathways (Moncrieffe et al., 2026). Our observations suggest that palmitoylation influences ER- and trans-Golgi network-associated localization of TRIF, indicating that this modification may regulate the spatial organization of TRIF required for signaling complex assembly. This spatial regulation provides a plausible mechanism by which palmitoylation could modulate not only TRIF-RIPK3 complex formation but also additional TRIF-dependent outputs. Although the present study defines the role of palmitoylation in necroptotic signaling, whether this modification also modulates interferon induction, inflammatory transcriptional programs, or canonical TLR3/TLR4 responses remains to be determined.

Several limitations should be considered. 2-BP is a broad-spectrum inhibitor of protein palmitoylation and cannot selectively block *Lc*zDHHC20b-mediated modification of TRIF. This issue is particularly relevant in the context of necroptosis because RIPK1 and MLKL have also been reported to undergo palmitoylation in mammalian systems (Pradhan et al., 2024; Zhang et al., 2024b). Although equivalent modifications have not yet been established in teleosts, 2-BP may affect multiple palmitoylation-sensitive steps within the necroptotic machinery rather than acting exclusively through the *Lc*zDHHC20b-TRIF axis. The 2-BP experiments should therefore be interpreted as supportive rather than definitive. Nevertheless, our conclusion is strengthened by convergent genetic and biochemical evidence, including *Lc*zDHHC20b knockdown, reduced TRIF palmitoylation, impaired TRIF-RIPK3 interaction, and site-directed *Lc*TRIF palmitoylation. A more definitive test would involve rescue or re-expression of palmitoylation-deficient TRIF mutants in primary large yellow croaker MO/MΦ. Such experiments were attempted, but repeated optimization using multiple transfection strategies did not achieve sufficient overexpression efficiency in this primary cell system for reliable functional evaluation. Thus, although the current data strongly support a role for TRIF palmitoylation in necroptosis, more robust TRIF mutant-based rescue analyses will be important for future studies.

In summary, this study identified *Lc*zDHHC20b-mediated TRIF palmitoylation as a previously unknown mechanism that drives necroptosis during bacterial infection in teleost fish. These findings establish TRIF as a palmitoylated protein for the first time in vertebrates and expand the functional repertoire of zDHHC20-family enzymes in innate immunity. Given the conserved architecture of TRIF-dependent signaling and necroptotic effectors, this study has broad implications for understanding lipid-based regulation of immune signaling and may inform therapeutic strategies targeting palmitoylation pathways in infectious and inflammatory diseases.

DATA AVAILABILITY

The mass spectrometry proteomics data generated in this study have been deposited in the ProteomeXchange Consortium via the PRIDE partner repository with the dataset identifier PXD065712 and Science Data Bank under accession number 31253.11.sciencedb.j00139.00299.

SUPPLEMENTARY DATA

Supplementary data to this article can be found online.

COMPETING INTERESTS

The authors declare that they have no competing interests.

AUTHORS' CONTRIBUTIONS

Z.Y.Z.: Investigation, Methodology, Visualization, Writing-original draft. C.J.F.: Investigation, Visualization, Writing-review & editing, Methodology. T.F.Z.: Investigation, Methodology, Writing-review & editing. J.Z.S. and X.Z.S.: Writing-review & editing. L.N.: Investigation, Visualization, Methodology, Conceptualization, Funding acquisition, Project administration, Supervision, Writing-review & editing. J.C.: Writing-review & editing, Conceptualization, Project administration, Supervision. All authors read and approved the final version of the manuscript.

REFERENCES

Abramson J, Adler J, Dunger J, et al. 2024. Accurate structure prediction of biomolecular interactions with AlphaFold 3. *Nature*, **630**(8016): 493–500.

Chamberlain LH, Shipston MJ. 2015. The physiology of protein *S*-acylation. *Physiological Reviews*, **95**(2): 341–376.

Chen BE, Sun Y, Niu JX, et al. 2018. Protein lipidation in cell signaling and diseases: function, regulation, and therapeutic opportunities. *Cell Chemical Biology*, **25**(7): 817–831.

Chen XR, Shi W, Wang F, et al. 2014. Zinc finger DHHC-type containing 13 regulates fate specification of ectoderm and mesoderm cell lineages by modulating Smad6 activity. *Stem Cells and Development*, **23**(16): 1899–1909.

Dai T, Zhao ZY, Zhu TF, et al. 2024. The anti-inflammatory role of zDHHC23 through the promotion of macrophage M2 polarization and macrophage necroptosis in large yellow croaker (*Larimichthys crocea*). *Frontiers in Immunology*, **15**: 1401626.

Dhuriya YK, Sharma D. 2018. Necroptosis: a regulated inflammatory mode of cell death. *Journal of Neuroinflammation*, **15**(1): 199.

Ding C, Shi X, Guan YL, et al. 2021. Deoxynivalenol induces carp neutrophil apoptosis and necroptosis via CYP450s/ROS/PI3K/AKT pathway. *Aquaculture*, **545**: 737182.

Draper JM, Smith CD. 2010. DHHC20: a human palmitoyl acyltransferase that causes cellular transformation. *Molecular Membrane Biology*, **27**(2-3): 123–136.

Fang C, Deng LB, Keller CA, et al. 2006. GODZ-mediated palmitoylation of $GABA_A$ receptors is required for normal assembly and function of GABAergic inhibitory synapses. *The Journal of Neuroscience*, **26**(49): 12758–12768.

Fukata M, Fukata Y, Adesnik H, et al. 2004. Identification of PSD-95 palmitoylating enzymes. *Neuron*, **44**(6): 987–996.

Gottlieb CD, Linder ME. 2017. Structure and function of DHHC protein *S*-acyltransferases. *Biochemical Society Transactions*, **45**(4): 923–928.

Greaves J, Carmichael JA, Chamberlain LH. 2011. The palmitoyl transferase DHHC2 targets a dynamic membrane cycling pathway: regulation by a C-terminal domain. *Molecular Biology of the Cell*, **22**(11): 1887–1895.

Hao KW, Xu H, Jiang S, et al. 2024. *Paralichthys olivaceus* MLKL-mediated necroptosis is activated by RIPK1/3 and involved in anti-microbial immunity. *Frontiers in Immunology*, **15**: 1348866.

He Y, Zeng MY, Yang DH, et al. 2016. NEK7 is an essential mediator of NLRP3 activation downstream of potassium efflux. *Nature*, **530**(7590): 354–357.

Hu J, Zhang F, Xu XJ, et al. 2014. Isolation, identification and virulence of the pathogen of white-spots disease in internal organs of *Pseudosciaena crocea*. *Oceanologia et Limnologia Sinica*, **45**(2): 409–417. (in Chinese)

Jiang H, Zhang XY, Chen X, et al. 2018. Protein lipidation: occurrence, mechanisms, biological functions, and enabling technologies. *Chemical Reviews*, **118**(3): 919–988.

Kaiser WJ, Sridharan H, Huang CZ, et al. 2013. Toll-like receptor 3-mediated necrosis via TRIF, RIP3, and MLKL. *Journal of Biological Chemistry*, **288**(43): 31268–31279.

Keklik G. 2023. Understanding evolutionary relationships and analysis methods through mega software. *International Journal of New Horizons in the Sciences*, **1**(2): 83–90.

Khan N, Lawlor KE, Murphy JM, et al. 2014. More to life than death: molecular determinants of necroptotic and non-necroptotic RIP3 kinase signaling. *Current Opinion in Immunology*, **26**: 76–89.

Khoury GA, Baliban RC, Floudas CA. 2011. Proteome-wide post-translational modification statistics: frequency analysis and curation of the Swiss-Prot database. *Scientific Reports*, **1**(1): 90.

Kumar S, Stecher G, Suleski M, et al. 2024. MEGA12: molecular evolutionary genetic analysis version 12 for adaptive and green computing. *Molecular Biology and Evolution*, **41**(12): msae263.

Li CH, Chen J, Nie L, et al. 2020a. MOSPD2 is a receptor mediating the LEAP-2 effect on monocytes/macrophages in a teleost, *Boleophthalmus pectinirostris*. *Zoological Research*, **41**(6): 644–655.

Li JY, Wang YY, Shao T, et al. 2020b. The zebrafish NLRP3 inflammasome has functional roles in ASC-dependent interleukin-1β maturation and gasdermin E-mediated pyroptosis. *Journal of Biological Chemistry*, **295**(4): 1120–1141.

Lu B, Sun YY, Chen BY, et al. 2024. zDHHC20-driven S-palmitoylation of CD80 is required for its costimulatory function. *Acta Pharmacologica Sinica*, **45**(6): 1214–1223.

Mateo-Tórtola M, Hochheiser IV, Grga J, et al. 2023. Non-decameric NLRP3 forms an MTOC-independent inflammasome. *BioRxiv*, doi: https://doi.org/10.1101/2023.07.07.548075.

Mesquita FS, Abrami L, Linder ME, et al. 2024. Mechanisms and functions of protein S-acylation. *Nature Reviews Molecular Cell Biology*, **25**(6): 488–509.

Moncrieffe MC, Suresh P, Boyle J, et al. 2026. Toll-like receptor signaling outcome is determined by the stoichiometry of the endogenous TRIFosome. *Science Advances*, **12**(10): eaeb9507.

Newton K. 2015. RIPK1 and RIPK3: critical regulators of inflammation and cell death. *Trends in Cell Biology*, **25**(6): 347–353.

Newton K, Manning G. 2016. Necroptosis and inflammation. *Annual Review of Biochemistry*, **85**: 743–763.

Nie L, Cai SY, Sun J, et al. 2019. MicroRNA-155 promotes pro-inflammatory functions and augments apoptosis of monocytes/macrophages during *Vibrio anguillarum* infection in ayu, *Plecoglossus altivelis*. *Fish & Shellfish Immunology*, **86**: 70–81.

Nie L, Wu XY, Zhao ZY, et al. 2025. Palmitoylation-mediated NLRP3 inflammasome activation in teleosts highlights evolutionary divergence in immune regulation. *Zoological Research*, **46**(1): 3–14.

Ning YJ, Lu XJ, Chen J. 2018. Molecular characterization of a tissue factor gene from ayu: a pro-inflammatory mediator via regulating monocytes/macrophages. *Developmental & Comparative Immunology*, **84**: 37–47.

Ocasio CA, Baggelaar MP, Sipthorp J, et al. 2024. A palmitoyl transferase chemical–genetic system to map ZDHHC-specific *S*-acylation. *Nature Biotechnology*, **42**(10): 1548–1558.

Osipovitch M, Lambrecht M, Baker C, et al. 2015. Automated protein motif generation in the structure-based protein function prediction tool ProMOL. *Journal of Structural and Functional Genomics*, **16**(3-4): 101–111.

Philippe JM, Jenkins PM. 2019. Spatial organization of palmitoyl acyl transferases governs substrate localization and function. *Molecular Membrane Biology*, **35**(1): 60–75.

Politis EG, Roth AF, Davis NG. 2005. Transmembrane topology of the protein palmitoyl transferase akr1. *Journal of Biological Chemistry*, **280**(11): 10156–10163.

Pradhan AJ, Chitkara S, Ramirez RX, et al. 2024. Acylation of MLKL impacts its function in necroptosis. *ACS Chem Biol*, **19**(2): 407–418.

Punta M, Coggill PC, Eberhardt RY, et al. 2012. The Pfam protein families database. *Nucleic Acids Research*, **40**(D1): D290–D301.

Qi ZT, Yan D, Xiong F, et al. 2021. Progresses of bcl-2 proteins in teleost

fish and mammals. *Acta Hydrobiologica Sinica*, **45**(4): 935–944. (in Chinese)

Rana MS, Kumar P, Lee CJ, et al. 2018. Fatty acyl recognition and transfer by an integral membrane *S*-acyltransferase. *Science*, **359**(6372): eaao6326.

Ren Y, Liu SF, Nie L, et al. 2019. Involvement of ayu NOD2 in NF-κB and MAPK signaling pathways: insights into functional conservation of NOD2 in antibacterial innate immunity. *Zoological Research*, **40**(2): 77–88.

Runkle KB, Kharbanda A, Stypulkowski E, et al. 2016. Inhibition of DHHC20-mediated EGFR palmitoylation creates a dependence on EGFR signaling. *Molecular Cell*, **62**(3): 385–396.

Shang S, Liu J, Hua F. 2022. Protein acylation: mechanisms, biological functions and therapeutic targets. *Signal Transduction and Targeted Therapy*, **7**(1): 396.

Shen HX, Lu XJ, Lu JF, et al. 2020. Beta-adrenergic receptor stimulation influences the function of monocytes/macrophages in ayu (*Plecoglossus altivelis*). *Developmental & Comparative Immunology*, **103**: 103513.

Shi W, Chen XR, Wang F, et al. 2016. ZDHHC16 modulates FGF/ERK dependent proliferation of neural stem/progenitor cells in the zebrafish telencephalon. *Developmental Neurobiology*, **76**(9): 1014–1028.

Shi W, Wang FR, Gao M, et al. 2015. ZDHHC17 promotes axon outgrowth by regulating TrkA-tubulin complex formation. *Molecular and Cellular Neuroscience*, **68**: 194–202.

Stix R, Lee CJ, Faraldo-Gómez JD, et al. 2020. Structure and mechanism of DHHC protein acyltransferases. *Journal of Molecular Biology*, **432**(18): 4983–4998.

Tang BY, Kang W, Dong Q, et al. 2024. Research progress on S-palmitoylation modification mediated by the ZDHHC family in glioblastoma. *Frontiers in Cell and Developmental Biology*, **12**: 1413708.

Tomić G, Sheridan C, Refermat AY, et al. 2024. Palmitoyl transferase ZDHHC20 promotes pancreatic cancer metastasis. *Cell Reports*, **43**(5): 114224.

Wang F, Chen XR, Shi W, et al. 2015. Zdhhc15b Regulates differentiation of diencephalic dopaminergic neurons in zebrafish. *Journal of Cellular Biochemistry*, **116**(12): 2980–2991.

Wu XY, Xiong JB, Fei CJ, et al. 2022. Prior exposure to ciprofloxacin disrupts intestinal homeostasis and predisposes ayu (*Plecoglossus altivelis*) to subsequent *Pseudomonas plecoglossicida*-induced infection. *Zoological Research*, **43**(4): 648–665.

Xu XW, Li MF, Wu Z, et al. 2017. Endoplasmic reticulum transmembrane proteins ZDHHC1 and STING both act as direct adaptors for IRF3 activation in teleost. *The Journal of Immunology*, **199**(10): 3623–3633.

Zaballa ME, van der Goot FG. 2018. The molecular era of protein S-acylation: spotlight on structure, mechanisms, and dynamics. *Critical Reviews in Biochemistry and Molecular Biology*, **53**(4): 420–451.

Zhang H, Sun Y, Wang Z, et al. 2024a. ZDHHC20-mediated S-palmitoylation of YTHDF3 stabilizes MYC mRNA to promote pancreatic cancer progression. *Nature Communications*, **15**(1): 4642.

Zhang N, Liu JP, Guo R, et al. 2024b. Palmitoylation licenses RIPK1 kinase activity and cytotoxicity in the TNF pathway. *Molecular Cell*, **84**(22): 4419–4435. e10.

Zhang N, Yang YX, Xu DC. 2025. Emerging roles of palmitoylation in pyroptosis. *Trends in Cell Biology*, **35**(6): 500–514.

Zhou BH, Hao QY, Liang YM, et al. 2023. Protein palmitoylation in cancer: molecular functions and therapeutic potential. *Molecular Oncology*, **17**(1): 3–26.